

submitted to the Astrophysical Journal

Evidence for a massive BH in the S0 galaxy NGC 4342

Nicolas Cretton

Leiden Observatory, PO Box 9513, 2300 RA Leiden, The Netherlands

Frank C. van den Bosch¹

Department of Astronomy, University of Washington, Seattle, WA 98195, USA²

arXiv:astro-ph/9805324v1 26 May 1998

¹Hubble Fellow

²Previously at Leiden Observatory, PO Box 9513, 2300 RA Leiden, The Netherlands.

ABSTRACT

We present axisymmetric dynamical models of the edge-on S0 galaxy NGC 4342. This small low-luminosity galaxy harbors, in addition to its outer disk, a bright nuclear stellar disk. A combination of observations from the ground and with the Hubble Space Telescope (HST) has shown that NGC 4342 rotates rapidly and has a strong central increase in velocity dispersion.

We construct simple two-integral Jeans models as well as fully general, three-integral models. The latter are built using a modified version of Schwarzschild’s orbit-superposition technique developed by Rix et al. and Cretton et al. These models allow us to reproduce the full line-of-sight velocity distributions, or ‘velocity profiles’ (VPs), which we parameterize by a Gauss-Hermite series. The modeling takes seeing convolution and pixel binning into account.

The two-integral Jeans models suggest a black hole (BH) mass between 3 and $6 \times 10^8 M_\odot$, depending on the data set used to constrain the model, but they fail to fit the details of the observed kinematics. The three-integral models can fit all ground-based and HST data simultaneously, but only when a central BH is included. Models without BH are ruled out to a confidence level better than 99.73 per cent. We determine a BH mass of $3.0_{-1.0}^{+1.7} \times 10^8 M_\odot$, where the errors are the formal 68.3 per cent confidence levels. This corresponds to 2.6 per cent of the total mass of the bulge, making NGC 4342 one of the galaxies with the highest BH mass to bulge mass ratio currently known.

The models that best fit the data do not have a two-integral phase-space distribution function. They have rather complex dynamical structures: the velocity anisotropies are strong functions of radius reflecting the multi-component structure of this galaxy.

When no central BH is included the best fit model tries to fit the high central velocity dispersion by placing stars on radial orbits. The high rotation velocities measured, however, restrict the amount of radial anisotropy such that the central velocity dispersion measured with the HST can only be fit when a massive BH is included in the models.

Subject headings: black hole physics — galaxies: elliptical and lenticular, cD — galaxies: individual (NGC 4342) — galaxies: kinematics and dynamics — galaxies: nuclei — galaxies: structure.

1. Introduction

Several lines of evidence suggest that active galactic nuclei (AGNs) are powered by accretion onto a super-massive black hole (BH) (Lynden-Bell 1969; Rees 1984). The much higher volume-number density of AGNs observed at redshift $z \approx 2$ than at $z = 0$, suggests that many quiescent (or ‘normal’) galaxies today must have gone through an active phase in the past, and therefore harbor a massive BH as well. Such a BH will significantly influence the dynamics of the galaxy inside a radius of influence, $r_{\text{BH}} = GM_{\text{BH}}/\sigma^2$, where σ is a characteristic velocity dispersion of the stars in the center. In particular, hydrostatic equilibrium requires that the rms velocities of the stars surrounding a massive BH follow an $r^{-1/2}$ power-law (Bahcall & Wolf 1976; Young 1980).

Since the late 70s, combined imaging and spectroscopy of the central regions of galaxies has suggested that massive BHs should be present in a number of early-type galaxies (see Kormendy & Richstone 1995 for a review). Conclusive dynamical evidence for the presence of a central BH requires that a model with a BH can fit all observations (photometric and kinematic), and that no model without a BH can provide an equally good fit. Such conclusive evidence can only be inferred from observations that probe well inside the radius where the BH dominates the dynamics. Up to a few years ago, most claimed BH detections were based on observations with spatial resolutions of similar size as the radii of influence of the inferred BH masses (Rix 1993). This, together with the limited amount of freedom in the models used to interpret the data, has hampered an unambiguous proof for the presence of these BHs (i.e., the observed kinematics could not be confronted with all possible dynamical configurations without a BH). Often spherical models were used even when the observed flattening was significant. If the models were axisymmetric, the distribution function (hereafter DF) was often assumed to depend only on the two classical integrals of motion, energy and vertical angular momentum; $f = f(E, L_z)$. This implies that the velocity dispersions in the radial and vertical directions are equal (i.e., $\sigma_R = \sigma_z$). It is well-known that strong radial anisotropy in the center of a galaxy results in a high central velocity dispersion, mimicking the presence of a massive BH (cf. Binney & Mamon 1982). Conclusive evidence for a BH therefore requires that one can rule out radial anisotropy as the cause of the high velocity dispersions measured, and models must thus be sufficiently general.

Recently two major breakthroughs have initiated a new era in the search for massive BHs in normal galaxies. First of all, we can now obtain kinematics at much higher spatial resolution (down to FWHM $\sim 0.1''$), using specially-designed spectrographs, such as the Subarcsecond Imaging Spectrograph (SIS) on the Canada-France Hawaii Telescope, or the Faint Object Spectrograph (FOS) and STIS aboard the HST. This allows us to probe the gravitational potential much closer to the center, where the BH dominates the dynamics. Not only has this improved the evidence for massive BHs in several old BH-candidate galaxies (M31, Ford et al. 1998; M32, van der Marel et al. 1997, 1998; M87, Harms et al. 1994, Macchetto et al. 1997; NGC 3115, Kormendy et al. 1996a; NGC 4594, Kormendy et al. 1996b), but it has also provided new cases (M84, Bower et al. 1998; NGC 3377, Kormendy et al. 1998; NGC 3379, Gebhardt et al. 1998; NGC 4261, Ferrarese, Ford & Jaffe 1996; NGC 4486B, Kormendy et al. 1997; NGC 6251, Ferrarese, Ford & Jaffe 1998; and NGC 7052, van der Marel & van den Bosch 1998). Secondly, the revolutionary increase in computer power has made it possible to investigate a large number of fully general,

three-integral models based on the orbit-superposition method (Schwarzschild 1979). In the past decade, this method has been used to build a variety of spherical, axisymmetric and triaxial models (e.g., Schwarzschild 1982; Pfenniger 1984; Richstone & Tremaine 1984, 1988; Zhao 1996). Levison & Richstone (1985), Richstone & Tremaine (1985), and Pfenniger (1984) showed how to include rotation velocities and velocity dispersions as kinematic constraints. More recently, Rix et al. (1997) and Cretton et al. (1998) extended this modeling technique even further by fitting to the *entire* velocity profiles (see also Richstone 1997). Van der Marel et al. (1997, 1998) used this to build fully general, axisymmetric models of M32, and showed convincingly that M32 harbors a massive BH. Recent review papers on this rapidly evolving field include Ford et al. (1998), Ho (1998), Richstone (1998), and van der Marel (1998).

In many galaxies where the presence of a BH has been suggested, a nuclear disk, seen close to edge-on, is present. These disks are either in gaseous form (M84, M87, NGC 4261, NGC 4594, NGC 6251, NGC 7052), or made up of stars (NGC 3115). It is easier to detect BHs in edge-on systems with disks, where one can use both the measured rotation velocities and the velocity dispersions to determine the central mass density. It is therefore not surprising that BHs have predominantly been found in galaxies with nuclear disks. Furthermore, nuclear disks allow a good determination of the central mass density of their host galaxies. Gaseous disks have the advantage that their kinematics can be easily measured from emission lines. Since gas in a steady-state disk can only move on non-intersecting orbits, the measured rotation velocities of a settled gas disk, in the equatorial plane of an axisymmetric potential, correspond to the circular velocities, $V_c(R) = \sqrt{Rd\Phi/dR}$. The rotation curve of a nuclear gas disk therefore provides a direct measure of the central potential gradient, and thus of the central mass density. However, often the gas disks are not in a steady state; many show a distorted morphology (e.g. M87, see Ford et al. 1994), and non-gravitational motion, such as outflow, inflow or turbulence can be present and complicate the dynamical analysis (e.g., NGC 4261, Jaffe et al. 1996; NGC 7052, van den Bosch & van der Marel 1995). Nuclear *stellar* disks do not suffer from this, but have the disadvantage that their kinematics are much harder to measure. First of all, the kinematics have to be determined from absorption lines rather than emission lines, and secondly, the line-of-sight velocity distributions, or velocity profiles (VPs), measured are ‘contaminated’ by light from the bulge component. However, van den Bosch & de Zeeuw (1996) showed that with sufficient spatial and spectral resolution one can resolve the VPs in a broad bulge-component and a narrow disk-component. From these VPs the rotation curve of the nuclear disk can be derived, providing an accurate measure for the central mass density. Therefore, galaxies with an embedded nuclear disk (either gaseous or stellar) observed close to edge-on are ideal systems to investigate the presence of massive BHs.

In this paper we discuss the case of NGC 4342; a small, low-luminosity ($M_B = -17.47$) S0 galaxy in the Virgo cluster. The galaxy is listed as IC 3256 in both the Second and Third Reference Catalogues of Bright Galaxies, since in the past it has occasionally been confused with NGC 4341 and NGC 4343 (see Zwicky & Herzog 1966). At a projected distance of $\sim 30''$ SE of NGC 4342, a small galaxy is visible. It is uncertain whether this is a real companion of NGC 4342 or whether it is merely close in projection. HST images of NGC 4342 revealed both an outer disk, as well as a very bright nuclear stellar disk inside $\sim 1''$ (van den Bosch et al. 1994; Scorza & van den Bosch 1998). It is a normal galaxy, with no detected ISM (Roberts et al. 1991), and with small

color-gradients (van den Bosch, Jaffe & van der Marel 1998, hereafter BJM98). For its size and luminosity, it does however reveal a remarkably large central velocity dispersion and a very steep rotation-curve (see BJM98). Unfortunately, the spectral resolution of the available kinematic data is insufficient to actually resolve the VPs in disk and bulge components. In order to determine the central mass density in NGC 4342, we thus have to construct dynamical models of the entire system: bulge and disk components. Here we present simple two-integral Jeans models as well as fully general three-integral models, and we provide evidence for the presence of a central massive dark object (MDO) of $\sim 3 \times 10^8 M_\odot$. Throughout this paper we assume the MDO to be a BH, but we discuss alternatives in Section 7.2

In Section 2 we briefly discuss the data used to constrain the models and in Section 3 we describe our mass model. In Section 4 we show the results of some simple two-integral modeling, and we discuss its shortcomings. Section 5 describes the general outline of the three-integral modeling technique. In Section 6 we discuss shortcomings of the velocity-profile parameterization used when applied to dynamically cold systems, and present a modified approach. The results of the three-integral modeling are discussed in Section 7. Finally, in Section 8, we sum up and present our conclusions. Throughout this paper we adopt a distance of 15 Mpc for NGC 4342, consistent with the distance of the Virgo cluster (Jacoby, Ciardullo & Ford 1990).

2. The data

All data used in this paper are presented and discussed in detail in BJM98. Here we merely summarize.

2.1. Photometric data

BJM98 used the Wide Field and Planetary Camera 2 (WFPC2) aboard the HST to obtain U , V and I band photometry of NGC 4342. The spatial resolution of these images is limited by the HST Point Spread Function (FWHM $\sim 0.1''$) and the size of the pixels ($0.0455'' \times 0.0455''$). The full field-of-view covers about $35'' \times 35''$. Figure 1 shows contour plots at two different scales of the I -band image. The presence of the nuclear disk is evident from the highly flattened, disk-like isophotes inside $1.0''$.

2.2. Kinematic data

Using the ISIS spectrograph mounted at the 4.2m William Herschel Telescope (WHT) at La Palma, BJM98 obtained long-slit spectra of NGC 4342 along both the major and the minor axis. The spectra have a resolution of $\sigma_{\text{instr}} = 9 \text{ km s}^{-1}$, and were obtained with a slit width of $1.0''$ under good seeing conditions with a PSF FWHM of $0.80''$ (major axis) and $0.95''$ (minor axis). After standard reduction, the parameters $(\gamma, V, \sigma, h_3, h_4)$ that best fit the VPs were determined using

the method described in van der Marel (1994). These parameters quantify the Gauss-Hermite (GH) expansion of the velocity profile $\mathcal{L}(v)$ as introduced by van der Marel & Franx (1993):

$$\mathcal{L}(v) = \frac{\gamma}{\sigma} \alpha(w) \left(1 + \sum_{j=3}^4 h_j H_j(w) \right), \quad (1)$$

where

$$w \equiv (v - V)/\sigma, \quad (2)$$

and

$$\alpha(w) = \frac{1}{\sqrt{2\pi}} e^{-\frac{1}{2}w^2}. \quad (3)$$

Here v is the line-of-sight velocity, H_j are the Hermite polynomials of degree j , and h_j are the Gauss-Hermite coefficients. The first term in equation (1) represents a Gaussian with line strength γ , mean radial velocity V , and velocity dispersion σ . The even GH-coefficients quantify symmetric deviations of the VP from the best-fitting Gaussian, and the odd coefficients quantify the asymmetric deviations.

We have averaged the kinematic WHT data at positive and negative radii. In this way we obtain sets of (V, σ, h_3, h_4) at 19 different positions along the major axis and 8 along the minor axis.

BJM98 also obtained FOS spectra at 7 different aperture-positions, all inside the central $0.5''$ of NGC 4342, using the circular $0.26''$ -diameter aperture (the FOS 0.3-aperture). Due to the limited signal-to-noise ratio (S/N) of these spectra, only (γ, V, σ) of the best-fitting Gaussian could be determined. Rotation velocities and velocity dispersions along the major axis of NGC 4342 for both the WHT (crosses) and FOS (solid dots) are shown in Figure 2. The central rotation gradient, as measured with the FOS, is extremely steep ($V \sim 200 \text{ km s}^{-1}$ at $0.25''$ from the center). In addition, the velocity dispersion increases from $\sim 90 \text{ km s}^{-1}$ at the outside (the ‘cold’ outer disk) to 317 km s^{-1} in the center as measured with the WHT. The central velocity dispersion increases to 418 km s^{-1} , when observed at four times higher spatial resolution with the FOS.

3. The mass model

We have used the Multi-Gaussian Expansion (MGE) method developed by Emsellem, Monnet & Bacon (1994, hereafter EMB94) to build a mass model for NGC 4342. The method assumes that both the PSF and the intrinsic surface brightness are described by a sum of Gaussians, each of which has 6 free parameters: the center (x_j, y_j) , the position angle, the flattening q'_j , the central intensity I'_j , and the size of the Gaussian along the major axis, expressed by its standard deviation a'_j . The best-fitting parameters of the different Gaussians are determined using an iterative approach in which additional components are added until convergence is achieved (see EMB94 for details on the method). This method is well suited for complicated, multi-component galaxies such as NGC 4342.

We fitted the HST I -band PSF by a sum of 5 circular (i.e., $q'_j = 1$) Gaussians (see BJM98). Using this model PSF we derived the parameters of the N Gaussians describing the intrinsic surface brightness (i.e., deconvolved for PSF effects) by fitting to the HST I -band image of NGC 4342. We forced the N Gaussians to have the same position angle and center, which yields an axisymmetric mass model (see below). Therefore, the model is described by $3N + 3$ free parameters, which are simultaneously fit to the image. We achieved convergence with $N = 11$ Gaussian components. The results of the fit are shown in Figure 1, where we show contour plots of the I -band image with superimposed contours of the convolved surface brightness of the MGE model. The fit is excellent, except for a small discrepancy at the outside. This is due to slight twisting of the isophotes at large radii (see BJM98). Since our model is axisymmetric, this cannot be modeled. Nevertheless, the discrepancy is small, and is unlikely to affect our conclusions on the dynamics of the central region. The parameters of the different Gaussian components are listed in Table 1.

The total luminosity of the MGE model in the I -band is $L_I = 3.57 \times 10^9 L_\odot$. This yields $M_I = -19.86$. The absolute blue magnitude of NGC 4342, at a distance of 15 Mpc, is $M_B = -17.47$ (Sandage & Tammann 1981), and we thus find $B - I = 2.39$. This is consistent with the colors of NGC 4342 presented by BJM98. They find $U - V \approx 1.5$ and $V - I \approx 1.3$. We thus derive $B - V \approx 1.09$, in good agreement with the average value for early-type galaxies (Faber et al. 1989). If we assume that the luminosity distribution of the bulge corresponds to the Gaussian components rounder than $q'_j = 0.3$, we find that the bulge makes up ~ 52 per cent of the total luminosity of NGC 4342. The outer disk, described by Gaussian components 9 and 10, makes up an additional 46.5 per cent, and the nuclear disk (modeled by Gaussian component 4) adds only about 1.5 per cent to the total luminosity. There is no reason that the mathematical components correspond to actual physical components, but at least this gives an order-of-magnitude description of the luminosities of the bulge and the two disk components. A more accurate disk-bulge decomposition, which yields similar results, is discussed in Scorza & van den Bosch (1998).

Assuming that the density is built up from a sum of three-dimensional Gaussians stratified on spheroids, one can, for any inclination angle i , analytically calculate the density distribution from the MGE fit to the intrinsic surface brightness. The mass density of such an MGE model is given by

$$\rho(R, z) = \Upsilon \sum_j I_j \exp \left[-\frac{1}{2a_j^2} \left(R^2 + \frac{z^2}{q_j^2} \right) \right], \quad (4)$$

where Υ is the mass-to-light ratio, and I_j , a_j and q_i are related to I'_j , a'_j , q'_j and i (see EMB94). The potential that corresponds to this density distribution follows from solving the Poisson equation. This yields

$$\Phi(R, z) = -4\pi G\Upsilon \sum_j a_j^2 q_j I_j \int_0^1 \exp \left[-\frac{t^2}{2a_j^2} \left(R^2 + \frac{z^2}{1 - e_j^2 t^2} \right) \right] \frac{dt}{\sqrt{1 - e_j^2 t^2}}, \quad (5)$$

where $e_j^2 = 1 - q_j^2$.

The inclination angle is well constrained by the thinness of the nuclear disk: $i > 83$ deg (Scorza & van den Bosch 1998). Throughout we assume that NGC 4342 is observed edge-on (i.e., $i = 90$ deg). Given the lower limit on the inclination angle of 83 deg, this assumption does not significantly influence the conclusions presented in this paper.

4. Jeans modeling

4.1. Formalism

The three-integral modeling described in the next section requires large amounts of CPU time. We therefore decided to first explore parameter space of the models (i.e., mass-to-light ratio and mass of the possible BH) by solving the Jeans equations and assuming that the phase-space distribution function depends only on the two classical integrals of motion. The Jeans equations for hydrostatic equilibrium are moment equations of the collisionless Boltzmann equation (see Binney & Tremaine 1987). They relate the velocity dispersion tensor $\hat{\sigma}^2$ and the streaming motion \mathbf{v} to the density ρ and potential Φ . For an axisymmetric system with distribution function $f(E, L_z)$ one always has $\sigma_R = \sigma_z$ and $\overline{v_R v_z} = 0$, and the Jeans equations in cylindrical coordinates reduce to

$$\frac{\partial(\rho\sigma_R^2)}{\partial R} + \rho\left(\frac{\sigma_R^2 - \overline{v_\phi^2}}{R} + \frac{\partial\Phi}{\partial R}\right) = 0, \quad (6)$$

$$\frac{\partial(\rho\sigma_z^2)}{\partial z} + \rho\frac{\partial\Phi}{\partial z} = 0. \quad (7)$$

Here $\overline{}$ denotes the local average over velocities. From equation (7) and $\rho(R, z)$ and $\Phi(R, z)$, one can, at every point (R, z) in the meridional plane, calculate $\sigma_R^2 (= \sigma_z^2)$ by simple integration. By rewriting equation (6), one can compute $\overline{v_\phi^2} = \overline{v_\phi^2} + \sigma_\phi^2$ without the need of performing a numerical (ill-conditioned) derivative (see e.g. Hunter 1977; Simien, Pellet & Monnet 1979; Binney, Davies & Illingworth 1990).

The expressions for σ_R^2 and $\overline{v_\phi^2}$ for the density distribution of equation (4) are given in EMB94 (their equations [42] and [44]). The Jeans equations do not prescribe how $\overline{v_\phi^2}$ splits in streaming motion $\overline{v_\phi}$ and azimuthal velocity dispersion σ_ϕ . We follow the approach introduced by Satoh (1980), and write

$$\overline{v_\phi} = k\sqrt{\overline{v_\phi^2} - \sigma_R^2}, \quad (8)$$

such that we can control the anisotropy σ_ϕ/σ_R by means of the free parameter k . For $k = 1$ the model is fully isotropic with $\sigma_\phi = \sigma_R = \sigma_z$. Once k has been fixed one can project the luminosity-weighted dynamical quantities on the plane of the sky (x', y') to yield the projected rotation velocities

$$V_{\text{rot}}(x', y') = \frac{-1}{S(x', y')} \int_{-\infty}^{\infty} \nu \overline{v_\phi} \sin i \cos \phi \, dz', \quad (9)$$

and the rms velocities

$$V_{\text{rms}}^2(x', y') = \frac{1}{S(x', y')} \int_{-\infty}^{\infty} \nu \left(\sigma_z^2 \cos^2 i + \sigma_R^2 \sin^2 \phi \sin^2 i + (\sigma_\phi^2 + \overline{v_\phi^2}) \cos^2 \phi \sin^2 i \right) dz'. \quad (10)$$

Here $\nu = \rho/\Upsilon$ is the luminosity density and $S(x', y')$ is the projected surface brightness at position (x', y') . V_{rot} and V_{rms}^2 are the true first and second order moments of the line-of-sight velocity distribution. The projected velocity dispersion $\sigma_p(x', y')$ is simply derived from

$$\sigma_p(x', y') = \sqrt{V_{\text{rms}}^2(x', y') - V_{\text{rot}}^2(x', y')}. \quad (11)$$

It is straightforward to include a BH in such a model, by simply adding $GM_{\text{BH}}/\sqrt{R^2 + z^2}$ to the stellar potential (5).

4.2. Application to NGC 4342

We use the Jeans equations to calculate the predicted rotation velocities and velocity dispersions for the luminosity distribution of NGC 4342. We assume that the stellar mass-to-light ratio Υ and the anisotropy parameter k are constant throughout the galaxy. We calculate V_{rot} and V_{rms}^2 (using equations [9] and [10]) on a two-dimensional grid on the sky. The grid is logarithmic in r (in order to properly sample the strong gradients near the center), and linearly sampled in θ . Once V_{rot} and V_{rms}^2 are tabulated, we convolve them with the PSF of the observations, weighted by the surface brightness. After pixel binning, taking the proper slit width into account, these are compared to the observations.

The V and σ determined from the GH fitting to the WHT VPs cannot be compared directly to V_{rot} and σ_p derived from the modeling discussed above: the latter ones correspond to the true moments of first and second order of the VPs, whereas the former ones correspond to the best-fitting Gaussian. We therefore recalculated the VP from V , σ , h_3 and h_4 , from which we then estimate the first and second order moments for direct comparison with the Jeans models.

The results are shown in Figure 3, where we plot V_{rot} , V_{rms} and σ_p of the VPs along the major axis for both the WHT and the FOS data. Also plotted are predictions for four models, that only differ in the mass of the central BH (0, 3, 5 and $10 \times 10^8 M_{\odot}$). All models have $i = 90$ deg, $\Upsilon_I = 6.2 M_{\odot}/L_{\odot}$ and $k = 1$ (i.e., all models are fully isotropic). For this value of k , we obtain the best fit to the observed velocity dispersion outside $\sim 2''$. However, V_{rot} is not very well fitted: the wiggles in the rotation curve are not reproduced by the model. One can alter k , as function of radius, such that we fit these wiggles, but at the cost of introducing them in the velocity dispersion profile. This is due to the poor fit of the Jeans models to the rms velocities (see lower-left panel of Figure 3). V_{rms}^2 depends only on the sum of σ_{ϕ}^2 and $\overline{v_{\phi}^2}$ (see equation [10]) and is therefore independent of k . Consequently, the Jeans models cannot simultaneously fit V_{rot} and σ_p along the major axis. This suggests that the assumption made, i.e., $f = f(E, L_z)$, is wrong, and that three-integral models are required.

The Jeans models without a central BH clearly underpredict the central velocity dispersion (for both the WHT and the FOS measurements), as well as the central rotation gradient measured with the FOS. Models with a massive BH provide a much better fit. The actual mass of the BH depends on the data set used to constrain the model: the WHT data suggests a BH mass of $\sim 3 \times 10^8 M_{\odot}$, whereas the FOS data are best fitted with $M_{\text{BH}} \approx 6 \times 10^8 M_{\odot}$. So although the

two-integral Jeans modeling cannot fit all the observed kinematics, it does suggest that a BH of a few times $10^8 M_\odot$ may be present in the center of NGC 4342.

In Figure 4 we plot the ratio of the observed rotation velocity over the rotation velocity of the best-fitting isotropic Jeans model, $V_{\text{obs}}/V_{\text{mod}}$ (along the major axis), versus the local observed ellipticity (in I -band) of NGC 4342. There is a clear correlation in the sense that the Jeans models underpredict the rotation velocity in the strongly flattened region, and overpredict V_{rot} in the less flattened region. The ellipticity is a measure of the local disk-to-bulge ratio, and this therefore suggests that disk and bulge have different velocity anisotropies. Since V_{rot} scales with $\sqrt{\Upsilon}$, another possibility may be that the disk and bulge are made up of different stellar populations (whose mass-to-light ratios are different by almost a factor two). However, the separate components (bulge, nuclear disk and outer disk) do not stand out as separate entities in either the $U - V$ or the $V - I$ color images (see BJM98), rendering this explanation improbable.

5. Three-integral modeling

In order to investigate the presence of a $\sim 3\text{--}6 \times 10^8 M_\odot$ BH as suggested by the Jeans models, we now construct fully general, axisymmetric models of NGC 4342. We use an extension of Schwarzschild’s (1979) orbit-superposition method (see de Zeeuw 1997), developed by Rix et al. (1997, hereafter R97) and Cretton et al. (1998, hereafter C98). The main method, but for spherical systems, is outlined in R97. The application to axisymmetric systems is discussed in C98. Here we briefly outline the method, and we refer the interested reader to R97 and C98 for details and tests of this modeling technique.

5.1. The method

The first step of the method is to integrate orbits in the combined potential $\Phi_{\text{stars}} + \Phi_{\text{BH}}$. Each orbit is then projected onto the space of observables, taking convolution with the PSF and pixel binning into account. Finally, a non-negative least-squares algorithm is used to determine the distribution of orbit weights that best fits the observational data (taking the observational errors into account), while also reproducing the luminous density distribution of the model.

Throughout we limit ourselves to models with an inclination angle $i = 90$ deg, and we assume that the stellar population has a constant mass-to-light ratio. Therefore, each model is characterized by only two free parameters: the mass-to-light ratio, Υ_I , and the mass of the black hole, M_{BH} . Our aim is to find the set $(M_{\text{BH}}, \Upsilon_I)$ that best fits the available constraints (surface brightness and velocity profiles).

5.2. The orbit library

The motion of a star in an axisymmetric potential, for which E and $L_z = Rv_\phi$ are conserved, can be reduced to motion in the meridional (R, z) -plane, in the effective potential $\Phi_e = \Phi(R, z) + L_z^2/(2R^2)$. The orbit is constrained within a region bounded by the zero velocity curve (ZVC) defined through $E = \Phi_e(R, z)$.

Each orbit in an axisymmetric potential $\Phi(R, z)$ admits two integrals of motion: energy $E = \Phi(R, z) + \frac{1}{2}v^2$ and vertical angular momentum $L_z = Rv_\phi$. Regular orbits admit one additional integral, I_3 , which in general is not known analytically. Such an orbit is confined to a sub-space inside the ZVC. We only found a very small fraction of our orbit catalog to be irregular.

The orbit library has to be set up such that one properly samples the full extent of phase space. The sampling has to be sufficiently dense to suppress discreteness noise, but is limited by the amount of available CPU time. After some testing we have chosen to calculate orbits on a $20 \times 20 \times 7$ (E, L_z, I_3)-grid. Each energy is uniquely defined by a circular radius R_c according to

$$E = \frac{1}{2}R_c \left. \frac{\partial \Phi}{\partial R} \right|_{R=R_c} + \Phi(R_c, 0). \quad (12)$$

The 20 energies are sampled logarithmically between $R_c(E) = 0.01''$ and $R_c(E) = 60''$. These values were chosen such as to encompass the major fraction of the total mass of the galaxy. The mass inside $R_c = 0.01''$ is only a fraction of 3.25×10^{-5} of the total mass, whereas a fraction of $\sim 2.85 \times 10^{-6}$ of the mass is located outside $R_c = 60''$. For each energy, we calculate the maximum vertical angular momentum

$$L_{z,\max}(E) = \sqrt{R_c^3 \left(\frac{\partial \Phi}{\partial R} \right)_{(R_c, 0)}}, \quad (13)$$

which corresponds to the circular orbit with energy E , and sample $|\eta| = |L_z|/L_{z,\max}$ on a linear grid of 10 values between 0.01 and 0.99. Hence, the purely circular and radial orbits are presumed to be represented by their closest neighbors on the grid, but are not explicitly calculated. At each value of $|\eta|$, only the orbit with positive angular momentum has to be integrated, since its counterpart ($L_z = -\eta L_{z,\max}$) is simply a mirror reflection around zero velocity. Since the third integral I_3 can generally not be expressed explicitly in terms of the phase-space coordinates, we use the method suggested by Levison & Richstone (1985), and take the starting point on the ZVC as a numerical representation of the third integral (see also C98). For that purpose we first calculate, for each (E, L_z) -pair, the locus (R_{tt}, z_{tt}) on the ZVC of the ‘thin tube orbit’. For a certain value of E and L_z , this is the only orbit that touches the ZVC at only one value of R . All other regular orbits touch the ZVC at two different values of R . We sample I_3 by linearly sampling the R -coordinate of the orbit’s starting point on the ZVC (R_{zvc}) between R_{tt} and R_{\max} , where R_{\max} is the maximum extent of the ZVC in the equatorial plane.

Since the calculation of the potential (equation [5]) and the forces all require the evaluation of a numerical quadrature, we have calculated them on a 4000×300 (R, θ) -grid in the meridional plane. The grid is sampled linearly in θ between 0 and $\pi/2$, and logarithmically in R between 10^{-4} and 10^3 arcseconds. Each orbit is integrated for 200 radial periods, using linear interpolation

between grid points to evaluate the potential and forces. On average, the energy conservation over 200 radial periods is better than one part in 10^5 , justifying the interpolation scheme adopted. In total $20 \times 10 \times 7 = 1400$ orbits are integrated, resulting in a library of $2 \times 1400 = 2800$ orbits (when doubling for the $-L_z$ orbits).

During the integration of each orbit we project its phase-space coordinates onto the space of observables (x', y', v_{los}) , where (x', y') is the plane on the sky, and v_{los} is the line-of-sight velocity. In the following we use v as shorthand for v_{los} . We adopt a three-dimensional grid in the (x', y', v) -space, i.e., our storage cube, in which we record the fractional time the orbit spends in each of the cells (see R97 for details). Once the orbit integration is finished, we convolve each of the velocity slices (x', y') with the PSF appropriate for the observations. Since we have kinematic constraints obtained with three different instrumental setups and different PSFs (WHT major axis, WHT minor axis, and FOS apertures) we use three separate (x', y', v) -storage cubes each of which is convolved with the respective PSF. We use two cubes with $0.1'' \times 0.1''$ (x', y') -cells for the WHT major and minor axes. For the FOS-cube, $0.05'' \times 0.05''$ cells are used to comply with the higher spatial resolution of the HST. For all storage cubes we use 101 velocity bins of 30 km s^{-1} . The final step is to calculate the contribution of the orbit to each of the positions in the plane of the sky where we have photometric and/or kinematic constraints. These positions are in general extended areas (e.g., determined by the pixel size of the CCD, the slit width and the pixel rebinning used to obtain spectra of sufficient S/N). For each constraint position $l = 1, \dots, N_c$ we therefore sum the fractional times over the area of l (see R97 for details). This gives us in the end, for each orbit k and each constraint position l , the properly PSF-convolved velocity profile ‘histogram’ $\text{VP}_{l,v}^k$, integrated over the area of position l . By using *fractional* times we ensure that each orbit is normalized to unity.

5.3. The observational constraints

The final step of the orbit-superposition method is to find the set of non-negative weights, γ_k , of each orbit that best matches the kinematic constraints and reproduces the luminous mass density of the model. Since we normalize each orbit to unity, the orbital weights γ_k measure the fraction of the total light of the galaxy that resides on orbit k . We use the following sets of constraints:

The solution γ has to reproduce the luminosity density $\rho(R, z)/\Upsilon$ (equation [4]). We have subdivided the first quadrant of the meridional plane in 20×7 (r, θ) -cells, with r and θ the standard spherical coordinates. The grid that encompasses those cells is binned linearly in θ , and logarithmically in r between $0.01''$ and $60''$. For each orbit k we store the fractional time t_n^k spent in cell n . Since we integrate the orbits in the meridional plane, this is similar to the fractional time the orbit spends in the three-dimensional volume obtained by integrating the area of the cell over 2π radians in the ϕ -direction. Therefore we have computed the total luminosity, L_n , of the MGE model inside each volume n . We will refer to these constraints as the “self-consistency constraints”.

From the WHT spectra we obtained sets of $(V_l, \sigma_l, h_{3,l}, h_{4,l})$ at 19 positions l along the major axis, and 8 along the minor axis. The quantities are the luminosity-weighted averages over the areas of constraint positions $l = 1, \dots, 27$. For each of these 27 positions we have calculated the surface brightness S_l integrated over that area, and convolved with the appropriate PSF. The quantities $S_l, V_l, \sigma_l, h_{3,l}$ and $h_{4,l}$ parameterize the velocity profiles $\mathcal{L}_l^{\text{obs}}(v)$ with

$$S_l = \int_{-\infty}^{\infty} \mathcal{L}_l^{\text{obs}}(v) dv. \quad (14)$$

One can rewrite this parameterization in the form $(S_l, S_l h_{1,l}, S_l h_{2,l}, S_l h_{3,l}, S_l h_{4,l})$, with

$$S_l h_{m,l} = 2\sqrt{\pi} \int_{-\infty}^{\infty} \mathcal{L}_l^{\text{obs}}(v) \alpha(w_l) H_m(w_l) dv, \quad (15)$$

where $m = 1, \dots, 4$, α is again the standard Gaussian (see equation [3]), and

$$w_l = \frac{v - V_l}{\sigma_l}, \quad (16)$$

with V_l and σ_l the measured rotation velocity and velocity dispersion of the VP's best-fitting Gaussian at constraint position l . Note that with this definition, $h_{1,l}$ and $h_{2,l}$ are zero for all constraint positions. This parameterization has the advantage that the orbit-superposition problem for the orbit weights is linear (see R97).

In addition, we obtained (V_l, σ_l) at 7 FOS aperture-positions. Again we have calculated, for each of these positions l , the PSF-convolved, aperture-integrated surface brightness S_l . The PSF used and the aperture diameter adopted are described in BJM98. As for the WHT spectra, we use the parameterization $(S_l, S_l h_{m,l})$ with $m = 1, 2$ as constraints rather than (S_l, V_l, σ_l) .

In total we thus have 140 self-consistency constraints L_n , 34 constraints on projected surface brightness S_l , and 122 kinematic constraints $S_l h_{m,l}$.

5.4. Non-negative least squares fitting

At each constraint position l we have a measured velocity profile $\mathcal{L}_l^{\text{obs}}(v)$, which we parameterized by $(S_l, S_l h_{m,l})$. For each of the observational constraints, we have the measurement errors $\Delta S_l, \Delta V_l, \Delta \sigma_l, \Delta h_{3,l}$ and $\Delta h_{4,l}$ from which we can calculate the errors $\Delta(S_l h_{m,l})$. As described in Section 5.2 we determined, for each orbit k and each position l , the velocity profile $\text{VP}_{l,v}^k$ at velocity v . We parameterize each orbital VP by $(S_l^k, S_l^k h_{m,l}^k)$ with $m = 1, \dots, 4$ using equations (14) and (15) and with $\mathcal{L}_l^{\text{obs}}(v)$ replaced by $\text{VP}_{l,v}^k$, and by changing the integration to a summation over all velocity bins. The orbit weights γ_k ($k = 1, \dots, N_{\text{orbits}}$) that result in the best fit to the observations can be determined by minimizing

$$\chi_{\text{obs}}^2 = \sum_l \left(\frac{S_l - \sum_k \gamma_k S_l^k}{\Delta S_l} \right)^2 + \sum_{m=1}^4 \sum_l \left(\frac{S_l h_{m,l} - \sum_k \gamma_k S_l^k h_{m,l}^k}{\Delta(S_l h_{m,l})} \right)^2. \quad (17)$$

In addition to minimizing χ_{obs}^2 , we also want the solution to match the luminosity density in the meridional plane, i.e., we also want to minimize

$$\chi_{\text{sc}}^2 = \sum_n \left(\frac{L_n - \sum_k \gamma_k t_n^k}{\Delta L_n} \right)^2, \quad (18)$$

where ΔL_n sets the accuracy for reproducing the luminosity density in the meridional plane. Throughout, we set $\Delta S_l = 0.01 S_l$ and $\Delta L_l = 0.01 L_l$, such that we aim for an accuracy of one per cent in reproducing both the projected PSF-convolved surface brightness and the luminosity density in the meridional plane. It is in principle sufficient to fit only the luminous density in the meridional plane: the surface brightness should be fitted automatically. However, because of discretization this is in practice not necessarily so, and we thus include the surface brightness at the constraint positions l as separate constraints.

Minimizing $\chi^2 \equiv \chi_{\text{obs}}^2 + \chi_{\text{sc}}^2$ is a least-squares problem for a matrix equation (see R97 for a detailed description of the matrices involved). It has to be solved under the physical constraint that $\gamma_k \geq 0$. Following Pfenninger (1984), R97 and C98, we use the Non-Negative Least Squares (NNLS) algorithm by Lawson & Hanson (1974) to solve for the orbit weights.

5.5. Regularization

The NNLS matrix equation solved is numerically rather ‘ill-conditioned’ giving rise to a distribution function with strong oscillatory behavior. Such DFs are unphysical (e.g., Lynden-Bell 1967; Spergel & Hernquist 1992; Merritt 1993). Smoothing in the solution space can be achieved via regularization (e.g., Merritt 1996 and references therein). We follow the scheme used by Zhao (1996), which is based on a minimization, up to a certain degree, of the differences in weights between neighboring orbits. The technique is described in R97, C98, and van der Marel et al. 1998, and we refer the interested reader to those papers for details. The extra regularization constraints result in a less good fit to the data. The amount of smoothing is set such that the regularized model is still compatible with the data in a statistical sense, i.e., such that $\Delta\chi^2 = \chi^2 - \chi_{\text{min}}^2 = 1$, with χ_{min}^2 the value obtained without regularization. Unless mentioned otherwise, we discuss results in which no regularization has been adopted.

6. Shortcoming of the Gauss-Hermite parameterization

Although the modeling technique outlined in the previous sections works well for dynamically hot galaxies (e.g. M32, see van der Marel et al. 1998), some problems arise when trying to apply it to dynamically cold systems such as NGC 4342. This is due to the fact that we do not include the zeroth-order moment h_0 in the fit. This quantity measures the normalization of the best-fitting Gaussian to the normalized VP and is observationally inaccessible: it is directly proportional to the unknown difference in line strength between the galaxy spectrum and the template spectrum used to analyze. (In practice one uses the assumption $h_0 = 1$ to estimate the line strength from

the observations.) As we now show, excluding h_0 from the GH series and expanding the orbital VPs around the observed VPs up to fourth order only, can lead to artificial counter-rotation in models of cold systems.

Assume we have an observed velocity profile VP_{obs} , at a certain position on the sky, that is perfectly Gaussian. The GH moments h_m with $m > 0$ of such a VP_{obs} will all be zero. In the method described above, we derive the orbital h_m^k ($m = 1, \dots, 4$) from equation (15) in which the observed V and σ enter in the weighting function $\alpha(w)H_m(w)$. In the NNLS algorithm we solve for the orbit weights by minimizing the difference between the GH moments of VP_{obs} and VP_{orb} . In principle, the differences between the $S_l h_{m,l}$ and $\sum_k \gamma_k S_l^k h_{m,l}^k$ are minimized, but for simplicity we illustrate the problem with a one-orbit model.

In the ideal case, an orbit whose VP deviates more strongly from the observed VP will be assigned a smaller weight. However, this is not always the case with the VP parameterization described in Section 5.3. To illustrate this we calculated the GH moments h_m ($m = 0, \dots, 2$) of a Gaussian expanded around another Gaussian, both with the same dispersion σ . In Figure 5 we plot the resulting moments h_m as function of the velocity difference ΔV between the two Gaussians (in units of σ). For $\Delta V = 0$, $h_0 = 1$ and all higher-order moments are zero (i.e., the two Gaussians are identical). In the regime $|\Delta V|/\sigma \lesssim 2$ the higher-order moments increase with increasing velocity-difference. For larger values of $|\Delta V|/\sigma$ they start to decrease again to reach approximately zero for $|\Delta V|/\sigma \gtrsim 5$. On the contrary, h_0 equals unity when the VPs are identical, and decreases monotonically for increasing $|\Delta V|/\sigma$.

In NGC 4342, which is a dynamically cold system, the major-axis kinematics reach $V_{\text{obs}}/\sigma_{\text{obs}} > 2.5$ at the outside (see Figure 6). An orbital VP with approximately the same V and σ as an observed VP with $V/\sigma > 2.5$ will have its h_1 and h_2 close to zero. Consequently, it will likely be given a non-zero weight. The same orbit, but with opposite sense of rotation (i.e., with reversed vertical angular momentum), will also have h_1 and h_2 close to zero, since $|\Delta V|/\sigma > 5$. In other words, the $+L_z$ and $-L_z$ orbits have the same S , h_1 and h_2 and are therefore indistinguishable for the fitting algorithm. The $+L_z$ and $-L_z$ orbits have opposite values of h_3 , but if $|h_3|$ is small, the difference between the two orbits, in terms of the VP parameterization used, remains small. If it would have been possible to include h_0 in the fit, then the $+L_z$ would have h_0 close to unity, and the $-L_z$ orbit would have $h_0 \approx 0$ (see Figure 5): the two VPs *would* have been easily distinguishable. In addition, if the observational data had been of sufficient S/N to derive GH moments up to very high order, it would also have been possible to distinguish the VPs of the $+L_z$ and $-L_z$ orbits. In practice, however, one requires unrealistic high S/N spectra to be able to measure these moments.

We can thus expect that our solutions will have significant amounts of counter-rotation at radii where $V_{\text{obs}}/\sigma_{\text{obs}} \gtrsim 2$. We indeed found solutions in which the reconstructed VPs at large radii along the major axis have two peaks at positive and negative v_{los} (see Section 7.1). Van der Marel et al. (1998) applied the same modeling technique to the dynamically hot system M32, which has $V/\sigma < 1.0$ everywhere, and therefore did not encounter this problem.

To solve the problem outlined above, we use a ‘modified approach’ in which we add some extra constraints to the models: we exclude counter-rotating orbits whose circular radius R_c is larger

than a limiting radius R_{lim} . We have chosen $R_{\text{lim}} = 4.5''$, since for larger radii $V_{\text{obs}}/\sigma_{\text{obs}} > 1.5$ (see Figure 6) and the VP parameterization used becomes poor in the light of the problem discussed above. As we show in Section 7.1, this solves the problem of the artificial counter-rotation at large radii along the major axis, but it has the disadvantage that our models are not fully general any more: we have imposed some a priori constraints on the amount of counter-rotating orbits in NGC 4342. On the other hand, the actual observations do not reveal any counter rotation at large radii. Critically, one may argue that the VP analysis of the spectra is not suitable to detect such counter rotation, since we do not go to sufficient high order in the GH expansion. We have therefore also analyzed our spectra with the unresolved Gaussian decomposition (UGD) method (Kuijken & Merrifield 1993), which is not hampered by this limitation (e.g., Merrifield & Kuijken 1994), and found good agreement with the results of the GH parameterization. This suggests that indeed NGC 4342 has a negligible amount of counter-rotating stars in its outer disk. The additional constraint imposed on the models, when using the modified approach, is thus justified observationally.

7. Results and discussion

7.1. The black hole and mass-to-light ratio

Based on the BH mass and mass-to-light ratio suggested by the Jeans modeling (Section 4.1) we construct three-integral models with M_{BH}/Υ_I in the range $0 - 1.5 \times 10^8 M_{\odot}$ and $4 \leq \Upsilon_I \leq 9$. For each value of M_{BH}/Υ_I only one orbit-library has to be constructed: a change in mass-to-light ratio is equivalent to a scaling of the model velocities proportional to $\sqrt{\Upsilon}$. We therefore calculate 10 different orbit libraries, all with $\Upsilon_I = 1$, that differ only in the mass of the central BH. If one scales to another value of Υ_I , the mass of the BH changes accordingly to $\Upsilon_I M_{\text{BH}}$. We sample the mass-to-light ratio at 16 different values in the interval $\Upsilon_I \in [4, 9]$.

For each of the in total 160 different $(M_{\text{BH}}, \Upsilon_I)$ -models we minimize $\chi^2 = \chi_{\text{obs}}^2 + \chi_{\text{sc}}^2$ (equations [17] and [18]). We use χ^2 statistics to compare different $(M_{\text{BH}}, \Upsilon_I)$ -models in a proper statistical way. We determine the measure $\Delta\chi^2 \equiv \chi^2 - \chi_{\text{min}}^2$, where χ_{min}^2 is the overall lowest χ^2 . Under the assumptions that the errors are normally distributed and that there are no numerical errors in the model, one can assign confidence levels to the measure $\Delta\chi^2$. The exact level of confidence depends on the number of degrees of freedom in the models (Press et al. 1992), in our case two: M_{BH} and Υ_I .

The resulting χ^2 -plots are shown in Figure 7. The first three contours show the formal 68.3, 95.4 and 99.73 per cent confidence levels (the latter one is plotted with a thick contour). The solid dots correspond to actual model calculations. Bi-cubic spline interpolation is used to calculate χ^2 at intermediate points. Four different plots are shown, labeled *a* to *d*. Plot *a* (upper-left panel) shows the χ^2 plot of the fits, when using only the V and σ measurements of the WHT spectra as constraints. Clearly, a large range of parameter space gives equally good fits. There is at best only a marginal indication that models with a BH fit the ground-based rotation velocities and velocity dispersions better than without a BH. Plot *b* (upper-right panel) is similar to plot *a*, except that

we have now included the h_3 and h_4 measurements of the WHT spectra as constraints on the models. Two changes are evident. First, the allowed range of Υ_I at given BH mass is much smaller. Secondly, BHs more massive than $\sim 6 \times 10^8 M_\odot$ can be ruled out at the 99.73 per cent confidence level. Plot *c* (lower-left panel) shows the resulting χ^2 -plot when all constraints, including the HST measurements are taken into account. These high spatial-resolution measurements allow us to rule out models without a BH at a confidence level better than 99.73 per cent. Finally, in plot *d* (lower-right panel) we show the results when using the modified approach on the entire set of constraints. As can be seen, the exclusion of counter-rotating orbits with circular radii beyond $4.5''$ puts some further limits on the allowed range of acceptable models, consequently contracting slightly the 99.73 per cent confidence region.

Although the solutions we find with the standard approach can result in models with significant counter-rotation (see Section 6), one can still meaningfully use the χ^2 statistics to put confidence levels on M_{BH} and Υ_I . The main requirement is that orbital VPs and observed VPs are parameterized in exactly the same way, which is the case. The counter rotation that we find is simply a consequence of our particular VP parameterization. Although the modified approach results in a more strict solution-space, and in principle is based on additional constraints that are observationally justified, we will nevertheless consider the χ^2 surface of Figure 7*c* as the main result. We merely present the results of the modified approach to show that the counter-rotation in the best-fitting models has no significant influence on the BH mass and mass-to-light ratio of our best-fitting model. Furthermore, Figure 7*c* results in more conservative estimates of the errors on BH mass and mass-to-light ratio.

The labeled asterisks in panel *c* indicate three models that will be discussed in more detail below. Model B provides the best overall fit and has $M_{\text{BH}} = 3.6 \times 10^8 M_\odot$ and $\Upsilon_I = 6.25 M_\odot / L_\odot$. From the χ^2 statistics we derive $M_{\text{BH}} = 3.0_{-1.0}^{+1.7} \times 10^8 M_\odot$ and $\Upsilon_I = 6.3_{-0.4}^{+0.5} M_\odot / L_\odot$. The errors are the formal 68.3 per cent confidence levels. For comparison, the modified approach yields $M_{\text{BH}} = 3.0_{-0.8}^{+0.9} \times 10^8 M_\odot$ and $\Upsilon_I = 6.5_{-0.3}^{+0.3} M_\odot / L_\odot$, which is consistent with and slightly more strict than the results obtained with the standard method.

Van der Marel et al. (1998) used the same three-integral modeling technique and statistical means to infer that M32 harbors a massive BH of $(3.4 \pm 0.7) \times 10^6 M_\odot$. To facilitate direct comparison, the χ^2 surfaces presented here are plotted with the same contour levels as in van der Marel et al. (1997, 1998). The χ^2 contours of Figure 7 correspond to the goodness-of-fit to *all* constraints. Van der Marel et al. plotted contours of χ^2 of the fit to the kinematic constraints only (i.e., the right term in equation [17]), but noted that contour plots of the total χ^2 look similar. We have computed the surfaces of the χ^2 that only measures the fit to the kinematic constraints and indeed found very similar contours: all models can fit the surface brightness and luminosity density to better than one per cent as requested.

In order to compare the kinematical predictions of the models with the actual observations, we compute the velocity profile of the model at each constraint position l , $\text{VP}_{l,v}$, as the weighted sum of all $\text{VP}_{l,v}^k$, using the solution γ for the orbit weights. For these VPs we then compute V_l and σ_l of the best-fitting Gaussian, as well as S_l and the GH moments $h_{3,l}$ and $h_{4,l}$, all of which can be directly compared to the observations. The kinematical predictions of models A, B and C

are plotted in Figure 8 together with the observations. Although we did not measure the h_3 and h_4 coefficients for the FOS spectra, we plot the model predictions for these quantities. All three models provide equally good fits to the projected surface brightness and the meridional luminosity density (not plotted). The main difference between models A and B is their fit to the central HST velocity dispersion. The model without BH (model A) underpredicts the observed dispersion by $\sim 130 \text{ km s}^{-1}$ ($\sim 4.0\Delta\sigma$). The rapid central rotation in NGC 4342, as measured with the FOS is remarkably well fit even without central BH. The main difference between models B and C is their fit to the central WHT velocity dispersion along the minor axis, and the fit to the h_3 measurements along the major axis. Although model C fits the central HST velocity dispersion even better than model B, the fit to the higher-order GH coefficients is worse to such an extent that this model can be ruled out to better than 99.73 per cent confidence (cf. panels *a* and *b* of Figure 7).

The large differences between the predictions of model C at the outermost point along the major axis (WHT measurements) and the actual observed values is due to the problem with the counter-rotation. This is illustrated in Figure 9, where we plot VPs at four different radii along the major axis. Solid dots represent the ‘observed’ velocity profiles, reconstructed from the measured GH-parameters (assuming that all GH coefficients of order five and higher are zero). The solid lines represent the reconstructed VPs of model C, and the dashed lines correspond to the Gauss-Hermite series fitted to these model VPs. The upper four panels show the VPs of model C. The lower panels show the VPs for a model with the same BH mass and mass-to-light ratio as model C, but for which the modified approach is used. For $R = 0.0''$ and $R = 4.83''$ the model VPs of the two different approaches are almost identical. However, for the larger radii, the VPs of model C clearly reveal large amounts of counter rotation. The VP of the upper-right panel has such a large counter-rotating component, that the best-fitting Gaussian no longer corresponds to the peak at positive velocities: it is very broad and centered around $V \approx 0 \text{ km s}^{-1}$. This causes the large difference between the model predictions and the observed values at the outermost WHT point in Figure 8. Although the reconstructed V and σ may differ strongly from the observed values, the h_1 and h_2 values are very similar. Since these are the values that enter into the computation of χ^2 , this discrepancy does not affect the χ^2 statistics.

It is interesting that the central velocity dispersions, as measured with the WHT, can be fit without the requirement of a central BH. This contradicts the conclusions reached from the Jeans modeling, which suggests, on the basis of the WHT measurements alone, that a BH of $\sim 3 \times 10^8 M_\odot$ is required. The three-integral modeling, however, shows that only the HST measurements are of sufficient spatial resolution to discriminate strongly between models with and without a massive BH (cf. panels *b* and *c* of Figure 7). Clearly, without these high spatial-resolution kinematics, the case for a BH is only marginal: the χ^2 plot in panel *b* of Figure 7 suggests a BH mass of $\sim 2.0 \times 10^8 M_\odot$, but cannot rule out models without a BH to a significant confidence level.

7.2. Alternatives to a black hole

7.2.1. A dense cluster

Although the dynamical evidence for the presence of a MDO of a few $10^8 M_\odot$ in NGC 4342 is compelling, it does not automatically imply evidence for a BH. Alternatives to a point mass, such as a cluster of brown dwarfs or stellar remnants are not ruled out by the modeling presented above. Any of these alternatives is only viable if its lifetime is not significantly smaller than the age of the galaxy (typically ~ 10 Gyr). There are three main processes that determine the evolution of a dense cluster: (i) core collapse, (ii) evaporation due to weak gravitational scattering, and (iii) physical collisions between the objects comprising the cluster. The latter of these processes is likely to ultimately lead to the formation of a single dense object, probably a massive BH. After a timescale τ_{coll} , each object has physically collided with another (in a statistical sense). τ_{coll} strongly depends on the mass and density of the cluster, as well as on the mass and size of the constituents (see Maoz 1997 and references therein). The characteristic timescale for evaporation of a cluster which consists of equal mass constituents is $\tau_{\text{evap}} \approx 300 \tau_{\text{relax}}$ (Spitzer & Thuan 1972), whereas typically after $\tau_{\text{cc}} \approx 16\tau_{\text{relax}}$, a Plummer sphere of equal mass objects undergoes core collapse (Cohn 1980). Here τ_{relax} is the median relaxation time (see Spitzer & Hart 1971). By choosing a Plummer model for the dark cluster we are conservative, in that more concentrated clusters have shorter collapse times, and are thus less likely as alternatives for a massive BH.

In order to constrain the size of a dark cluster, we construct models in which we replace the point-mass potential of the BH by a Plummer potential with a scale length ϵ . We consider model B for which we replace the $3.6 \times 10^8 M_\odot$ BH by a Plummer potential with the same mass, but with different values of ϵ . The stellar mass-to-light ratio is kept constant at 6.25. Figure 10 shows the resulting χ^2 as function of ϵ . The best fit is obtained for $\epsilon = 0.0$ (model B), and the fit deteriorates with increasing scalelength of the Plummer potential. The dotted line indicates the formal 99.73 per cent confidence level, and at this level of confidence we can rule out dark clusters with $\epsilon > 0.07''$. This upper limit on the scale length of the Plummer sphere corresponds to 5.1 pc at the assumed distance of 15 Mpc, implying a central density of the cluster $> 6.7 \times 10^5 M_\odot \text{pc}^{-3}$.

We calculate the relaxation timescale τ_{relax} , and the collision timescale τ_{coll} in which we adopt the mass-radius relation for *non-collapsed* objects used by Goodman & Lee (1989). In Figure 11 we plot the characteristic timescales for core-collapse and collisional destruction of our dark cluster, as function of the mass m of the cluster’s constituents. As can be seen, the timescales for core collapse ($\tau_{\text{cc}} \approx 7 \times 10^{11} (m/M_\odot)^{-1}$ yr) and evaporation ($\tau_{\text{evap}} \sim 20\tau_{\text{cc}}$) for the inferred dark cluster in NGC 4342 exceed the Hubble time for $m \lesssim \text{few } M_\odot$, and neither of these processes thus allows us to rule out a dark cluster as an alternative to a BH. The collision timescale τ_{coll} is the most restricting, and we are close to being able to rule out dark clusters of non-collapsed objects with masses less than $\sim 0.001 M_\odot$. However, for clusters of brown dwarfs with masses of $\sim 0.08 M_\odot$, τ_{coll} is still of the order of 10^{12} yr, and such clusters can clearly not be ruled out by current observations. Clusters of *collapsed* stellar remnants, such as white dwarfs or neutron stars, have collision timescales that are even much larger than the value of τ_{coll} plotted in Figure 11. This is due to the much smaller collisional cross-sections of these collapsed objects. In fact, the collapse time for a dark cluster can be made arbitrarily long by giving its objects an arbitrarily small mass, and the problems with collisions and mergers can be avoided by assuming the cluster

to be a collisionless gas of elementary particles. However, another effect might allow one to rule out such a dark cluster: the trapping of stars by the cluster due to dynamical friction. If the time scale for this process is smaller than the age of the galaxy, enough stars will get trapped such that the cluster can no longer be considered dark. Alternatively, these trapped stars can merge and form a massive BH, thus spoiling the goal for which the cluster was introduced. The time scale for the trapping to occur is independent of the mass m of the cluster constituents, but does depend on the mass m^* of the stars being captured, and is given by $(m/m^*)\tau_{cc}$ (as long as $m^* \gg m$, see Quinlan 1996). For NGC 4342 we thus find that this capture time scale is only smaller than $\sim 10^{10}$ yr for stars with $m^* \gtrsim 70 M_{\odot}$. We can thus not use this trapping-mechanism to put an appreciable constraint on the nature of a possible dark cluster in NGC 4342.

In conclusion, it is clear that we are still a long way from being able to rule out dark clusters as viable alternatives for a massive BH in the center of NGC 4342.

7.2.2. An end-on bar

It has been argued that a bar observed end-on may mimic the presence of a BH (Gerhard 1988). In particular, the nuclear disk in NGC 4342 may in fact be a (very thin) nuclear bar. However, there are several reasons why this interpretation is unlikely. First of all, axisymmetric models without BH fail to fit the central velocity dispersion, as measured with the HST/FOS, by $\sim 130 \text{ km s}^{-1}$. It seems unlikely that the elongated orbits in a bar potential can fix this. Furthermore, there are no indications that (the center of) NGC 4342 is triaxial. Although van den Bosch & Emsellem (1998) have provided evidence that NGC 4570, a galaxy with a double-disk morphology similar to NGC 4342, has been shaped under the influence of a rapidly tumbling bar-potential, none of the characteristics found in NGC 4570 that led to this conclusion are apparent in NGC 4342. In addition, no minor axis rotation is found, and the small amount of isophote twist observed (see BJM98) is limited to the outer region of the galaxy, and is more likely to be associated with a small warping of the outer disk, probably induced by the small companion at $\sim 30''$ SE. Finally, the steep cusp of the bulge of NGC 4342 makes the bar hypothesis unlikely, since the pressure support from this strongly cusped bulge probably assures stability against bar formation (cf. van den Bosch & de Zeeuw 1996).

7.3. The dynamical structure of NGC 4342

During the orbit integrations we store, in addition to the fractional time spent by orbit k in meridional cell n , t_n^k , the time-weighted first and second order velocity moments averaged over cell n . With the solution for the orbit weights γ we can compute the internal dynamical structure of the model averaged over each cell n . These are given by

$$\langle v_a \rangle_n = \frac{\sum_k \gamma_k t_n^k \langle v_a \rangle_n^k}{\sum_k \gamma_k t_n^k}, \quad (19)$$

and

$$\langle v_a^2 \rangle_n = \frac{\sum_k \gamma_k t_n^k \langle v_a^2 \rangle_n^k}{\sum_k \gamma_k t_n^k}. \quad (20)$$

Here we use the subscript a to indicate either of the cylindrical coordinates R , ϕ or z . The cell-averaged velocity dispersions can be computed according to $\langle \sigma_a \rangle_n^2 = \langle v_a^2 \rangle_n - \langle v_a \rangle_n^2$.

In order to suppress noise, we average $\langle v_a \rangle_n$ and $\langle v_a^2 \rangle_n$ over cells n that have the same radius r but different θ (r and θ being the standard spherical coordinates). Given the strongly flattened shape of NGC 4342 and its multi-component structure, we decided to split the galaxy in two parts: we determine the internal dynamical structure in two cones; one with half-opening angle of 30 deg centered around the equatorial plane, including the nuclear and outer disks, and the other one with half-opening angle of 60 deg centered around the minor axis, representing the bulge of NGC 4342.

We investigate the dynamical structure of models A, B, and C using the modified approach (see Section 6.1) and regularization as described in Section 5.5 in order to suppress noise. As a check, we compare the dynamical structures before and after regularization (with the amount of smoothing chosen such that $\Delta\chi^2 = 1$). The regularized model is found to have a smoother dynamical structure, but the main features are similar for both cases indicating that our results are not too sensitive to the particular method and amount of regularization adopted.

In Figure 12 we plot the dynamics in the ‘equatorial cone’ as function of radius. The upper panels show the rms velocities for models A, B and C in the range between $r = 0.1''$ and $r = 12''$ (corresponding to the regime where we have kinematic constraints along the major axis). The middle panels display the ratio $\sigma_a/\sigma_{\text{total}}$ for the same radial interval ($\sigma_{\text{total}}^2 = \sum_a \sigma_a^2$). Since there is no streaming motion in the radial and vertical directions, $\langle \sigma_R \rangle$ and $\langle \sigma_z \rangle$ are equal to their respective rms velocities. The difference between $\langle v_\phi^2 \rangle$ and σ_ϕ reflects the streaming motion of the model. The lower panels show the ratios σ_z/σ_R and σ_ϕ/σ_R . The three models differ predominantly in the inner $\sim 3.0''$, reflecting the differences in BH mass, but are very similar outside of $3.0''$: clearly $\langle v_\phi^2 \rangle$ dominates the dynamics outside this radius in accordance with the rapid rotation of the outer disk. The rapid change in dynamical structure (from azimuthally anisotropic to radially anisotropic) going from $3''$ to $12''$ reflects the strong increase of $(V/\sigma)_{\text{obs}}$ over this radial interval (see Figure 6): the dynamically cold outer disk, mainly built up of close-to-circular orbits with low σ_ϕ , becomes the dominant mass component. Over the same radial interval, the projected ellipticity increases from ~ 0.4 to ~ 0.7 , and this thus explains the observed correlation between ellipticity and $V_{\text{obs}}/V_{\text{mod}}$ of the best fitting isotropic Jeans model plotted in Figure 4. At $R \gtrsim 8''$, $\sigma_\phi/\sigma_R \sim 0.75$, not too different from the value in the solar neighborhood where $\sigma_\phi/\sigma_R = 0.6$ (Dehnen 1998).

Models B and C have σ_z/σ_R remarkably constant at ~ 0.9 , and are thus not too different from two-integral models (for which this ratio is exactly 1.0). This is very different from the case without BH (model A) for which σ_z/σ_R is a strong function of radius R . This is the reason that the two-integral, isotropic Jeans model discussed in Section 4, could not fit the HST rotation velocities without BH, whereas model A can.

The main change going from model A to model C, is a strong increase of σ_ϕ/σ_R in the

inner $\sim 3''$. In these inner regions the circular velocities increase strongly with increasing BH mass. Nevertheless, all three models provide an almost equally good fit to the observed rotation velocities. We checked our solutions and found that going from model A to C, the ratio of $-L_z$ -orbits over $+L_z$ -orbits increases in the radial interval $0.5'' < R < 3.0''$. This causes the net streaming motions of all three models to be roughly similar despite the large differences in circular velocities. Furthermore, it explains the strong increase in σ_ϕ observed when going from model A to model C.

The dynamics of the bulge (represented by the cone with half-opening angle of 60 deg centered around the minor axis) is presented in Figure 13. We only plot the results out to $R = 3.0''$, corresponding to the radial interval where we have kinematic constraints along the minor axis. At $R \gtrsim 1''$ the models are again similar, being dominated by rotation, albeit to a much lesser extent than along the major axis. Model A is radially anisotropic in the central region ($R \lesssim 1''$), and σ_R decreases steadily with BH mass going from model A to model C. The radial anisotropy of the central region of the bulge of model A is required to fit the high central velocity dispersions observed as good as possible. Close to the equatorial plane, the steep rotation curve observed prevents model A from being too radially anisotropic (see also Section 7.4). Model B is again remarkably close to two-integral form, having $\sigma_z/\sigma_R \sim 1.0$.

7.4. The influence of central radial anisotropy

We now investigate to what extent radial anisotropy can influence the central kinematics of NGC 4342. We solve the orbit weights for the model with $\Upsilon_I = 7.25 M_\odot/L_\odot$ and $M_{\text{BH}} = 0$ using two different sets of constraints. The first one uses all constraints except the *rotation velocities* measured with the FOS. The second one excludes only the FOS *velocity dispersions* from the constraints. The results for both models are shown in Figure 14, where we plot the predictions for the rotation velocities and velocity dispersions of both models. We only plot the predictions for the FOS kinematics: both models have almost indistinguishable WHT kinematics. The lower two panels in Figure 14 show the dynamics of the resulting models; we plot both $\langle v_R^2 \rangle^{1/2}$ and $\langle v_\phi^2 \rangle^{1/2}$ as function of radius. These quantities are averaged between $\theta = 0$ deg and $\theta = 90$ deg.

The model with the FOS rotation velocities excluded from the constraints (solid lines) reveals the highest central velocity dispersion achievable without a BH, while still fitting the WHT measurements. The model predicts a central rotation curve that is too shallow to fit the observed rotation velocities, and is strongly radially anisotropic in the center. The model excluding the FOS velocity dispersions (dashed lines) shows a very steep central rotation curve. The model is strongly azimuthally anisotropic in the center, resulting in a much smaller central velocity dispersion. Clearly, a model without a central BH cannot simultaneously fit the rotation velocities and velocity dispersions measured with the FOS.

7.5. The density distribution in the outer region of NGC 4342

The best-fitting mass-to-light ratio of $\Upsilon_I = 6.3M_\odot/L_\odot$ is unusually large for the stellar population of an early-type galaxy (e.g., van der Marel 1991). The mass-to-light ratio is mainly set by the large rotation velocities measured at the outside of NGC 4342 (along the major axis). The large value found may indicate that NGC 4342 is embedded in a massive dark halo. We did not attempt to include such a component for two reasons: First, we are mainly interested in trying to fit the central kinematics and to examine the mass of a possible BH. The characteristics of a possible dark halo will not affect the central dynamics, and therefore will not alter our main conclusion that NGC 4342 harbors a massive BH. It may however result in a different dynamical structure of the outer bulge and disk. Secondly, since we can fit all kinematics without having to infer a dark halo, including such a component in the models will merely lead to a large range of different models that can fit the observed kinematics equally well. Only kinematics at much larger radii can constrain the presence and characteristics of such a possible dark halo (cf. R97).

Since mass-to-light ratio scales with distance d as d^{-1} , another explanation for the large value of Υ_I derived might be an underestimate of the distance. In order to bring the inferred mass-to-light ratio in accordance with the average value for early-type galaxies, NGC 4342 has to be at about twice the assumed distance of 15 Mpc. This is however hard to reconcile with the observed heliocentric velocity of NGC 4342 of only 714 km s^{-1} (de Vaucouleurs et al. 1976). Galaxies out to 15 Mpc from the center of the Virgo cluster can still experience a Virgocentric infall of a few hundred km s^{-1} : our local group falls towards Virgo with $\sim 200 \text{ km s}^{-1}$ (Tammann & Sandage 1985). A distance of 30 Mpc for NGC 4342, however, would imply a Virgocentric infall velocity of $\sim 1500 \text{ km s}^{-1}$ (where we have taken Virgo to be at 1100 km s^{-1}), which seems too large. So, the small recession velocity of NGC 4342 implies that it can not be too far behind Virgo such as to have an appreciable effect on the inferred mass-to-light ratio.

Another problem related to the outer density distribution is that the mass model used (the MGE model) falls off as $\exp(-r^2)$ at large radii. This is probably not correct, but since we only have photometry that is limited to a small radial extent, we cannot examine this in more detail. The main requirement is that we have a proper mass model for the major part of the galaxy. Our MGE model has a total luminosity of $L_I = 3.57 \times 10^9 L_\odot$. We have shown in Section 3, that for this luminosity we derive $B - V = 1.09$, in good agreement with the average value for early-type galaxies. This therefore suggests that our MGE model covers the major part of the galaxy, and that the galaxy does not extend far beyond the radial extent of our MGE model. In addition, as is the case with a dark halo, a change in the luminosity density profile in the outer parts of NGC 4342 will not affect our main conclusions regarding the presence of a central BH.

7.6. Comparison with other BH detections

There are now about a dozen BH candidates known. The best cases are the center of the MW, where a proper-motion study has revealed a $2.5 \times 10^6 M_\odot$ BH (Eckart & Genzel 1997), and NGC 4258, where water masers are found to be in Keplerian rotation around a $3.6 \times 10^7 M_\odot$ BH

(Miyoshi et al. 1995). Other strong evidence for the existence of massive BHs comes from the observation of the Fe $K\alpha$ line at 6.4 keV in a number of Seyfert 1 nuclei: the X-ray emission line exhibits relativistic motions, interpreted as arising from the accretion disk surrounding a massive BH (Tanaka et al. 1995; Nandra et al. 1997).

Most other BH detections (or confirmations) are based on observations with the HST. Observations of nuclear gas disks with the HST has provided strong cases for massive BHs in M84, M87, NGC 4261, NGC 6251, and NGC 7052. All other cases are based on stellar dynamical evidence: M31, M32, NGC 3115, NGC 3377, NGC 3379, and NGC4486B. Of these only M 32, NGC 3379 and NGC 4342 discussed here have been confronted with three-integral modeling thus far. As discussed in Section 1, one can only hope to properly detect a BH if one can observe its kinematics inside r_{BH} . All currently detected BHs have $r_{\text{BH}} > 0.1''$, and since all these galaxies, except the nucleus of the Milky Way, have now been observed with the HST, all current BH-candidates fulfill this requirement. Remarkable enough, most of these galaxies (M31, M32, M87, NGC 3115, and NGC 4594) were already considered BH candidates when the angular resolution of the observations was still an order of magnitude larger, and similar to the angular size of the radius of influence of the inferred BH (Rix 1993). The BH in NGC 4342 has a relatively small radius of influence, with an angular size of $\sim 0.4''$. Indeed we have shown that only the HST/FOS observations are of sufficient spatial resolution to rule out models without a central BH.

Kormendy & Richstone (1995) have suggested a relation between the mass of the BH and that of the bulge of its parent galaxy: $\langle M_{\text{BH}}/M_{\text{bulge}} \rangle = 0.22^{+0.14}_{-0.09} \times 10^{-2}$. For more recent discussions on this relation, including more recent BH detections see Kormendy et al. (1998), Ho (1998), van der Marel (1998), and van der Marel & van den Bosch (1998). NGC 4342 is the galaxy with currently the second-highest ratio of BH mass over bulge mass of $2.6^{+1.5}_{-0.9} \times 10^{-2}$, and is only superseded by the peculiar galaxy NGC 4486B, for which the case of a massive BH is less strong (Kormendy et al. 1997). NGC 3115 ($M_{\text{BH}}/M_{\text{bulge}} = 2.4 \times 10^{-2}$) and the Milky Way ($M_{\text{BH}}/M_{\text{bulge}} = 0.017 \times 10^{-2}$) are other clear deviants. Clearly, the scatter around the suggested relation is considerable, seemingly as large as nearly two orders of magnitude.

8. Conclusions

Spectra obtained with the WHT and HST/FOS of the edge-on S0 galaxy NGC 4342 have revealed a very steep central rotation curve and a strong central increase in velocity dispersion. These data suggest a large central mass concentration. In this paper we presented detailed dynamical models of NGC 4342 used to investigate whether its nucleus harbors a massive BH.

We model the luminous density distribution of NGC 4342 with multiple Gaussian components. After projection and PSF convolution this model provides an excellent fit to the HST I -band surface brightness distribution. The parameters of this model were derived with the MGE method.

Simple isotropic Jeans models suggest that NGC 4342 harbors a massive BH of a few times $10^8 M_{\odot}$. The actual mass of the BH depends on the data-set fitted: the WHT data suggest $M_{\text{BH}} \approx 3 \times 10^8 M_{\odot}$; the HST/FOS data suggest a somewhat larger BH mass of $\sim 6 \times 10^8 M_{\odot}$. This

discrepancy already suggests that the assumptions underlying the Jeans models, i.e., $f = f(E, L_z)$ and therefore $\sigma_R = \sigma_z$, are incorrect. This is also evident from the fact that the Jeans models cannot accurately fit the major-axis rms velocities measured with the WHT. These rms velocities are independent of the freedom in the anisotropy σ_ϕ/σ_R allowed in the Jeans modeling. We find that for a mass-to-light ratio $\Upsilon_I = 6.2 M_\odot/L_\odot$ and an isotropic velocity distribution ($\sigma_R = \sigma_z = \sigma_\phi$) the Jeans model with $M_{\text{BH}} = 3 \times 10^8 M_\odot$ provides the best fit to the observed WHT velocity dispersions along the major axis. However, the rotation velocities are not very well fitted and we find a correlation between $V_{\text{obs}}/V_{\text{mod}}$ and the local ellipticity of the projected surface brightness, such that the model underpredicts the rotation velocities in the highly flattened regions (dominated by the disk light) and overpredicts them in the less flattened region (dominated by the bulge light). This suggests that the different components in NGC 4342 have different velocity anisotropies.

We thus constructed three-integral axisymmetric models of NGC 4342 in order to examine the mass of a possible BH and the dynamical structure of the different components. The modeling technique is an extension of Schwarzschild’s orbit-superposition technique, and is based on finding the ensemble of orbits that best fits the observations. These models make no assumption about the dynamical structure and are fully general. This technique, developed by Rix et al. (1997) and Cretton et al. (1998), has previously been used to prove the existence of a massive BH of $(3.4 \pm 0.7) \times 10^6 M_\odot$ in the compact elliptical M32 (van der Marel et al. 1998). We have constructed a range of dynamical ($M_{\text{BH}}, \Upsilon_I$)-models of NGC 4342 to determine a central BH mass of $3.0_{-1.0}^{+1.7} \times 10^8 M_\odot$ and an *I*-band mass-to-light ratio of $6.3_{-0.4}^{+0.5} M_\odot/L_\odot$. The high spatial resolution of the HST/FOS data allow us to rule out models without a BH to a confidence level better than 99.73 per cent. With a similar confidence we can rule out models with a BH more massive than $7 \times 10^8 M_\odot$. This upper limit on the BH mass is mainly due to the VP shape parameters h_3 and h_4 . With the current data we can not rule out alternatives to a massive BH, such as a cluster of brown dwarfs or stellar remnants. Nevertheless, the QSO paradigm, together with the fact that the presence of massive BHs in galactic nuclei has unambiguously been demonstrated in a few galaxies where the inferred central densities are high enough to rule out dark clusters as alternatives (see discussion in Maoz 1997), make the interpretation of the inferred MDO in NGC 4342 in terms of a massive BH the most likely.

We computed the intrinsic mean velocities and velocity dispersions of the three-integral models. The dynamical structures of the best fitting models vary strongly with radius, reflecting the multi-component structure of NGC 4342. Between $2''$ and $12''$ in the equatorial plane the best fitting models change from azimuthally anisotropic to radially anisotropic, while $\sigma_z/\sigma_R \approx 0.9$. This explains the correlation between the projected ellipticity and the failure of the isotropic Jeans models to fit the observed rotation velocities along the major axis. The bulge in the best fitting model without BH is radially anisotropic. However, we have shown that even without the constraints of the measured HST/FOS rotation velocities, models without BH cannot fit the central HST/FOS velocity dispersion. The rotation velocities measured from the ground already constrain the amount of central radial anisotropy such that models without a BH cannot fit the high central velocity dispersion measured with the HST/FOS.

The BH mass thus derived contributes a fraction of $2.6_{-0.9}^{+1.5}$ per cent to the total mass of the

bulge ($1.2 \times 10^{10} M_{\odot}$). With this BH mass, NGC 4342 has one of the highest ratios of BH mass over bulge mass. Currently, the BH in our own galaxy has, with 0.02 per cent, the lowest BH mass to bulge mass ratio known: the scatter in the M_{BH} vs. M_{bulge} relation seems to be as large as two orders of magnitude. Extremely high spatial resolution is required in order to investigate if other galaxies have even lower values of $M_{\text{BH}}/M_{\text{bulge}}$. In conclusion, current data are consistent with a relation between bulge mass and BH mass, but the scatter is very large, and it is likely that the current $M_{\text{BH}}/M_{\text{bulge}}$ ratios found are biased towards an upper limit. Although the newly installed Space Telescope Imaging Spectrograph (STIS) is likely to detect many more BH cases in the coming years, detection of BHs with masses of the order of a 0.02 per cent of the bulge mass or less in galaxies in Virgo or beyond, will probably have to await a next generation space telescope.

Part of the calculations presented in this paper were performed on two UltraSparcs, kindly made available by the Lorentz Center. Many thanks are due to Eric Emsellem, for his help with the MGE analysis, and to Tim de Zeeuw, Walter Jaffe, HongSheng Zhao and Roeland van der Marel for many fruitful discussions. FvdB was supported by a Hubble Fellowship, #HF-01102.11-97A, awarded by STScI. NC acknowledges the hospitality of Steward Observatory where part of this work was done.

REFERENCES

- Bahcall, J. N., & Wolf, R.A. 1976, *ApJ*, 209, 214
- Binney, J. J., & Mamon, G. A. 1982, *MNRAS*, 200, 361
- Binney, J. J., & Tremaine, S. D. 1987, *Galactic Dynamics*. (Princeton: Princeton University Press)
- Binney, J. J., Davies, R. L., & Illingworth, G. D. 1990, *ApJ*, 361, 78
- Bower, G. A., et al. 1998, *ApJ*, 492, L111
- Cretton, N., de Zeeuw, P. T., van der Marel, R. P., & Rix, H.-W. 1998, *ApJ*, submitted (C98)
- Cohn, H. 1980, *ApJ*, 150, 163
- Dehnen, W. 1998, preprint, astro-ph/9803110
- de Vaucouleurs, G., de Vaucouleurs, A., & Corwin, H. C. 1976, *Second Reference Catalogue of Bright Galaxies*. (University of Texas, Austin)
- de Zeeuw, P. T. 1997, in *The Nature of Elliptical Galaxies*, eds., M. Arnaboldi, G.S. Da Costa, P. Saha. ASP. Conference Series 116, p.44
- Eckart, A., & Genzel, R. 1997, *MNRAS*, 284, 576
- Emsellem, E., Monnet, G., & Bacon, R. 1994, *A&A*, 285, 723 (EMB94)
- Faber, S. M., Wegner, G., Burstein, D., Davies, R. L., Dressler, A., Lynden-Bell, D., & Terlevich, R. J. 1989, *ApJS*, 69, 763
- Ferrarese, L., Ford, H. C., & Jaffe, W. 1996, *ApJ*, 470, 444
- Ferrarese, L., Ford, H. C., & Jaffe, W. 1998, *ApJ*, in press
- Ford, H. C., et al. 1994, *ApJ*, 435, L27
- Ford, H. C., Tsvetanov, Z. I., Ferrarese, L., & Jaffe, W. 1998, in *IAU Symp. 184, The Central Regions of the Galaxy and Galaxies*, ed. Y. Sofue (Dordrecht: Kluwer), in press
- Gebhardt, K., et al. 1998, *AJ*, in press
- Gerhard, O. E. 1988, *MNRAS*, 232, 13P
- Goodman, J. & Lee, H. M. 1989, *ApJ*, 337, 84
- Harms, R. J., et al. 1994, *ApJ*, 435, L35
- Ho, L. C. 1998, in *Observational Evidence for Black Holes in the Universe*, ed. S. K. Chakrabarti (Dordrecht: Kluwer), in press (astro-ph/9803307)
- Hunter, C. 1977, *AJ*, 82, 271
- Jacoby, G. H., Ciardullo, R., & Ford, H. C. 1990, *ApJ*, 356, 332
- Jaffe, W., Ford, H. C., Ferrarese, L., van den Bosch, F. C., & O'Connell, R. W. 1996, *ApJ*, 460, 214
- Kormendy, J., & Richstone, D. 1995, *ARA&A*, 33, 581
- Kormendy, J., et al. 1996a, *ApJ*, 459, L57

- Kormendy, J., et al. 1996b, *ApJ*, 473, L91
- Kormendy, J., et al. 1997, *ApJ*, 482, L139
- Kormendy, J., Bender, R., Evans, A. S., & Richstone, D. 1998, *AJ*, in press
- Kuijken, K., & Merrifield, M. R. 1993, *MNRAS*, 264, 712
- Lawson, C. L., & Hanson, R. J. 1974, *Solving Least Squares Problems*. (Englewood Cliffs: New Jersey)
- Levison, H. F., & Richstone, D. O. 1985, *ApJ*, 295, 349
- Lynden-Bell, D. 1967, *MNRAS*, 136, 101
- Lynden-Bell, D. 1969, *Nature*, 223, 690
- Macchetto, F., Marconi, A., Axon, D. J., Capetti, A., Sparks, W. B., & Crane, P. 1997, *ApJ*, 489, 579
- Maoz, E. 1998, *ApJ*, 494, L181
- Merrifield, M. R., & Kuijken, K. 1994, *ApJ*, 432, 575
- Merritt, D. 1993, *ApJ*, 413, 79
- Merritt, D. 1996, *AJ*, 112, 1085
- Miyoshi, M., et al. 1995, *Nature*, 373, 127
- Nandra, K., George, I. M., Mushotzky, R. F., Turner, T. J., & Yaqoob, T. 1997, *ApJ*, 477, 602
- Pfenniger, D. 1984, *A&A*, 141, 171
- Press, W. H., Teukolsky, S. A., Vetterling, W. T., & Flannery, B. P. 1992, *Numerical Recipes*. (Cambridge University Press: Cambridge)
- Quinlan, G. D. 1996, *New Astronomy*, 1, 255
- Rees, M. J. 1984, *ARA&A*, 22, 471
- Richstone, D. O., & Tremaine, S. D. 1984, *ApJ*, 286, 27
- Richstone, D. O., & Tremaine, S. D. 1985, *ApJ*, 296, 370
- Richstone, D. O., & Tremaine, S. D. 1988, *ApJ*, 327, 82
- Richstone, D. O. 1997, in *The Nature of Elliptical Galaxies*, eds., M. Arnaboldi, G.S. Da Costa, P. Saha. ASP. Conference Series 116, p.123
- Richstone, D. O. 1998, in *IAU Symp. 184, The Central Regions of the Galaxy and Galaxies*, ed. Y. Sofue (Dordrecht: Kluwer), in press
- Rix, H.-W. 1993, in *IAU Symp. 153, Galactic Bulges*, eds., H. Dejonghe, & H.J. Habing. (Dordrecht: Kluwer), p. 423
- Rix, H.-W., de Zeeuw, P. T., Cretton, N., van der Marel, R. P., & Carollo, C. M. 1997, *ApJ*, 488, 702 (R97)
- Roberts, M. S., Hogg, D. E., Bregman, J. L., Forman, W. R., & Jones, C. 1991, *ApJS*, 75, 751

- Sandage, A., & Tammann, G. A. 1981, A Revised Shapley-Ames Catalogue of Bright Galaxies. (Carnegie Institute of Washington: Washington DC)
- Satoh, C. 1980. PASJ, 32, 41
- Schwarzschild, M. 1979, ApJ, 232, 236
- Schwarzschild, M. 1982, ApJ, 263, 599
- Scorza, C., & van den Bosch, F. C. 1998, MNRAS, in press
- Simien, F., Pellet, A., & Monnet, G. 1979, A&A, 72, 12
- Spergel, D. N., & Hernquist, L. 1992, ApJ, 397, L78
- Spitzer, L., & Hart, M. H. 1971, ApJ, 164, 399
- Spitzer, L., & Thuan, T. X. 1972, ApJ, 175, 31
- Tammann, G. A., & Sandage, A. 1985, ApJ, 294, 81
- Tanaka, Y., et al. 1995, Nature, 375, 659
- van den Bosch, F. C., Ferrarese, L., Jaffe, W., Ford, H. C., & O’Connell, R. W. 1994, AJ, 108, 1579
- van den Bosch, F. C., & van der Marel, R. P. 1995, MNRAS, 274, 884
- van den Bosch, F. C., & de Zeeuw, P. T. 1996, MNRAS, 283, 381
- van den Bosch, F. C., & Emsellem, E. 1998, MNRAS, in press, (astro-ph/9804039)
- van den Bosch, F. C., Jaffe, W., & van der Marel, R. P. 1998, MNRAS, 293, 343 (BJM98)
- van der Marel, R. P. 1991, MNRAS, 253, 710
- van der Marel, R. P. 1994, MNRAS, 270, 271
- van der Marel, R. P. 1998, in IAU Symp. 186, Galaxy Interactions at low and high Redshift, eds. D. B. Sanders & J. Barnes (Dordrecht: Kluwer), in press
- van der Marel, R. P., & Franx, M. 1993, ApJ, 407, 525
- van der Marel, R. P., & de Zeeuw, P. T., Rix, H.-W., & Quinlan, G. D. 1997, Nature, 385, 610
- van der Marel, R. P., Cretton, N., de Zeeuw, P. T., & Rix, H.-W., 1998, ApJ, 493, 613
- van der Marel, R. P., & van den Bosch, F. C. 1998, AJ, submitted, (astro-ph/9804194)
- Young, P. J. 1980, ApJ, 242 1232
- Zhao, H. S. 1996, MNRAS, 283, 149
- Zwicky, F., & Herzog, E. 1966, Catalogue of Galaxies and of Clusters of Galaxies, Vol. III. California Institute of Technology

Fig. 1.— Contour maps of the WFPC2 *I*-band image of NGC 4342 at two different scales: $32'' \times 32''$ (left-hand panel) and $8'' \times 8''$ (right-hand panel). Superimposed are the contours of the MGE model of the intrinsic surface brightness convolved with the HST PSF (see Section 3).

Fig. 2.— Observed rotation velocities V and velocity dispersions σ (as determined from the best-fitting Gaussian, see text) along the major axis of NGC 4342 obtained with the WHT (crosses) and the FOS (solid dots). The gradient of the rotation velocity and the central velocity dispersion increase considerably going to the four times higher spatial resolution of the FOS. See BJM98 for details on the data.

Fig. 3.— Results of the Jeans modeling. The solid dots with errorbars indicate the observed rotation velocities and velocity dispersions. Overplotted are four models that differ only in the mass of the central BH ($0, 3, 5$ and $10 \times 10^8 M_\odot$). All models have fully isotropic velocity dispersions, and a stellar mass-to-light ratio of $\Upsilon_I = 6.2 M_\odot/L_\odot$. The three panels on the left show the WHT kinematics and the model predictions for V_{rot} , σ_p and V_{rms} . The model with $M_{\text{BH}} = 3 \times 10^8 M_\odot$ provides the best fit to the velocity dispersions. Neither of the four models provides an accurate fit to the rotation velocities (see also Figure 4). The panels on the right compare the model predictions with the HST/FOS kinematics. Both the rotation velocities and the velocity dispersions suggest the presence of a BH with a mass of $\sim 6 \times 10^8 M_\odot$.

Fig. 4.— The ratio $V_{\text{obs}}/V_{\text{mod}}$ of the observed rotation velocities over the rotation velocities predicted by the isotropic Jeans model with $\Upsilon_I = 6.2 M_\odot/L_\odot$ and $M_{\text{BH}} = 3 \times 10^8 M_\odot$, as function of the local, projected ellipticity of the isophotes. Only results beyond $2''$ are shown. At smaller radii seeing influences the observed quantities significantly. There is a clear correlation in that the Jeans model underpredicts the rotation velocities in the moderately flattened region, and overpredicts the rotation velocities in the radial interval where the isophotes are strongly flattened, and thus dominated by the light of the outer disk component.

Fig. 5.— The Gauss-Hermite moments h_m ($m = 0, 1, 2$) of a Gaussian VP expanded around another Gaussian with the same dispersion σ . Results are plotted as functions of the velocity difference ΔV between the two Gaussians, expressed in units of σ . For $\Delta V = 0$, the two Gaussians are identical and $h_0 = 1$ and $h_m = 0$ ($m = 1, 2, 3, \dots$).

Fig. 6.— The ratio V/σ as function of radius of the major-axis kinematics of NGC 4342 as measured with the WHT (solid dots) and the HST/FOS (open circles). The dotted line indicates R_{lim} outside which $V/\sigma > 1.5$. In the modified approach, we exclude counter-rotating orbits with circular radii $R_c > R_{\text{lim}}$ from the NNLS.

Fig. 7.— Contour plots of $\chi^2 = \chi_{\text{obs}}^2 + \chi_{\text{sc}}^2$, which measures the goodness-of-fit to the constraints as function of BH mass, M_{BH} , and *I*-band mass-to-light ratio, Υ_I . The first three contours define the formal 68.3, 95.4 and 99.73 per cent confidence levels (latter one is plotted with a thick contour). The subsequent contours are characterized by a factor two increase in $\Delta\chi^2$. Solid dots indicate actual model calculations. The χ^2 surface of panel *a* results from excluding h_3 and h_4 as well as

all HST/FOS measurements from the constraints. In panel *b* we have only excluded the HST/FOS data, and panel *c* shows the resulting χ^2 plot when all constraints are taken into account. The asterisks labeled A, B and C indicate special models discussed in the text. Finally, in panel *d* we have used the modified approach and included the additional constraint that counter-rotating orbits with $R_c > 4.5''$ are not allowed in the solution.

Fig. 8.— Kinematics for the three data sets (solid dots with errorbars) compared to the predictions for models A (dotted lines), B (solid lines) and C (dashed lines). Although we did not measure h_3 and h_4 from our HST/FOS spectra, we plot the model predictions in the lower two panels on the right. Model A, which has no BH, strongly underestimates the central velocity dispersion as measured with the FOS. The strong deviation of the predictions of model C for the outermost WHT-point along the major axis, is due to the ‘artificial’ counter-rotation of the model (see Figure 9).

Fig. 9.— Velocity profiles at four different radii along the major axis of NGC 4342. The observed VPs, reconstructed from the measured V , σ , h_3 and h_4 while assuming $h_m = 0$ for $m \geq 5$, are plotted as solid dots. The solid lines correspond to the model VPs, and the dashed lines to the Gauss-Hermite series (up to order 4) fitted to these model VPs. Upper panels correspond to model C, whereas lower panels correspond to a model with the same BH mass and mass-to-light ratio, but whose orbit solution was computed with the modified approach. The upper panels clearly reveal that the model VPs at larger radii are double peaked. This can yield strange Gaussian fits, as evident from the upper right panel. The modified approach excludes counter-rotating orbits with $R_c > 4.5''$ from the orbit library, and does not reveal these double peaked VPs.

Fig. 10.— The value of $\chi^2 = \chi_{\text{obs}}^2 + \chi_{\text{sc}}^2$, which measures the goodness-of-fit to the constraints, as function of the scale length ϵ (in arcsec) of the Plummer potential with a total mass of $3.6 \times 10^8 M_\odot$ representing a cluster of dark objects in the center of NGC 4342. All models have a stellar mass-to-light ratio of 6.25. The best fit to the data is achieved in the limit $\epsilon \rightarrow 0$, which corresponds to our model with a BH rather than a dark cluster. We can rule out models with $\epsilon > 0.07''$ at the 99.73 per cent confidence level.

Fig. 11.— The timescales for core collapse (τ_{cc}) and collisional destruction (τ_{coll}) of a $3.6 \times 10^8 M_\odot$ Plummer cluster of non-collapsed objects with a central density of $6.7 \times 10^5 M_\odot \text{pc}^{-3}$ as function of the mass m of the constituents. If any of these timescales is less than $\sim 10^{10}$ years, it makes such cluster an unlikely alternative to a BH. Unfortunately, current data does not allow us to rule out any of the dark clusters as an alternative MDO in NGC 4342.

Fig. 12.— The dynamical structure of models A, B and C averaged over a cone with half-opening angle of 30 deg centered on the equatorial plane. Upper panels show the rms velocities $\langle v_a^2 \rangle^{1/2}$ in km s^{-1} , middle panel the normalized velocity dispersions $\sigma_a / \sigma_{\text{total}}$, and lower panels the ratios σ_a / σ_R . Solid curves are for the radial component ($a = R$), dotted curves for the azimuthal component ($a = \phi$), and dashed curves for the vertical component ($a = z$). Results are plotted over the radial interval where we have kinematic constraints along the major axis, i.e., $0.1'' < R < 12''$.

Fig. 13.— Same as Figure 12, except that here the quantities are averaged over a cone with half-opening angle of 60 deg centered on the symmetry axis ($R = 0$) of the models.

Fig. 14.— Radial velocity anisotropy at work: Solid lines are for a model with $\Upsilon_I = 7.25 M_\odot / L_\odot$ and $M_{\text{BH}} = 0$, where we have neglected the FOS measurements of the rotation velocities. The dashed lines correspond to the same model, but for which we have neglected the FOS velocity-dispersion measurements. The two lower panels show the intrinsic dynamics, $\langle v_R^2 \rangle^{1/2}$ (lower-left panel) and $\langle v_\phi^2 \rangle^{1/2}$ (lower-right panel), of the two models.

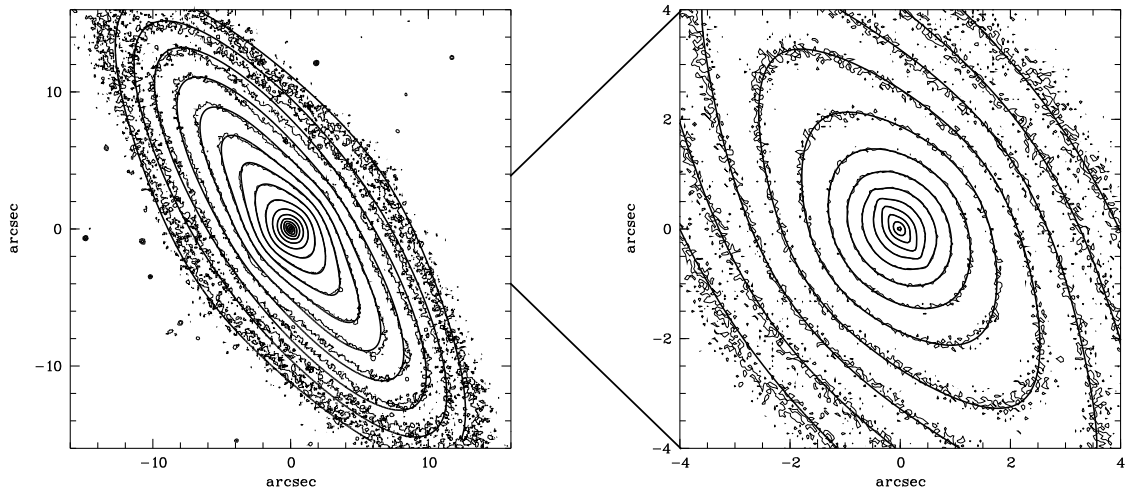


Figure 1

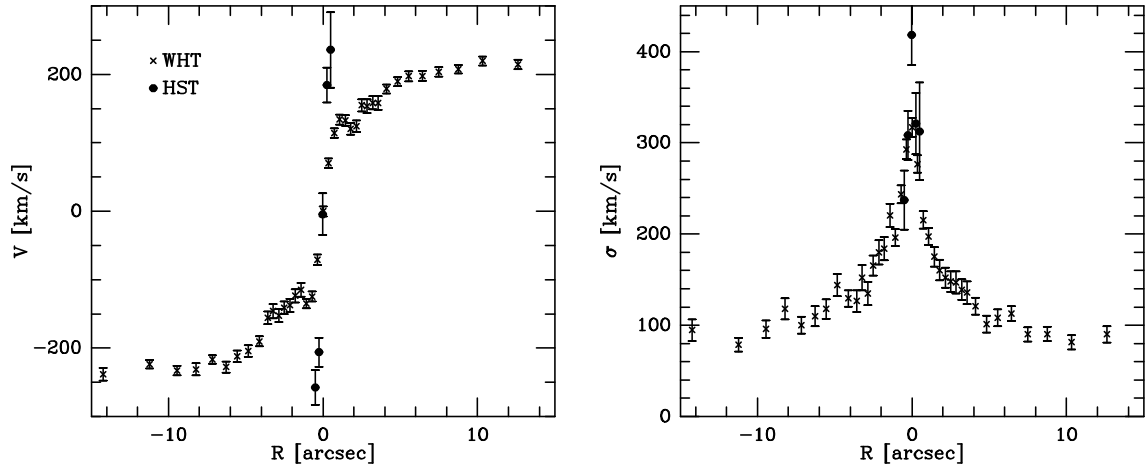


Figure 2

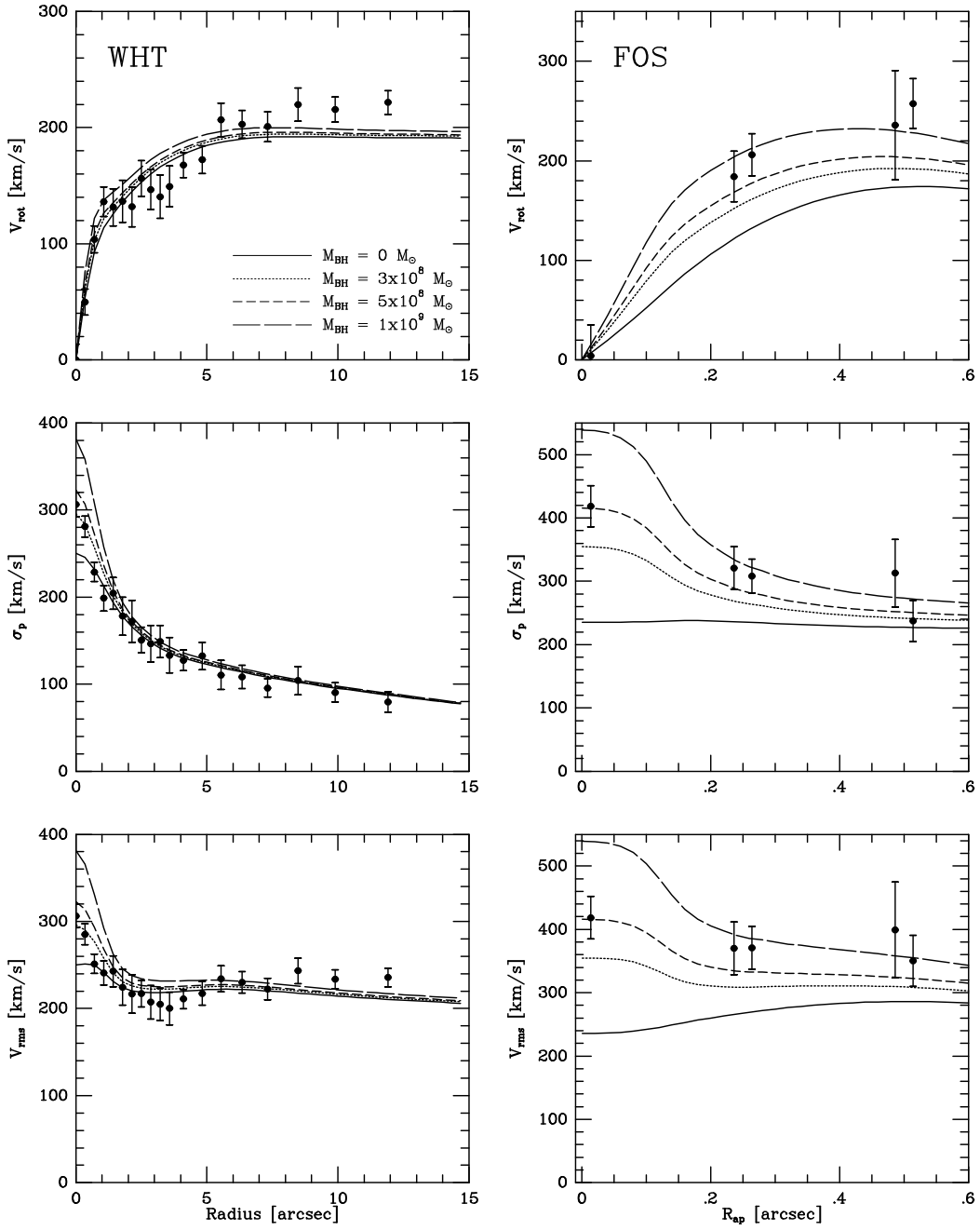


Figure 3

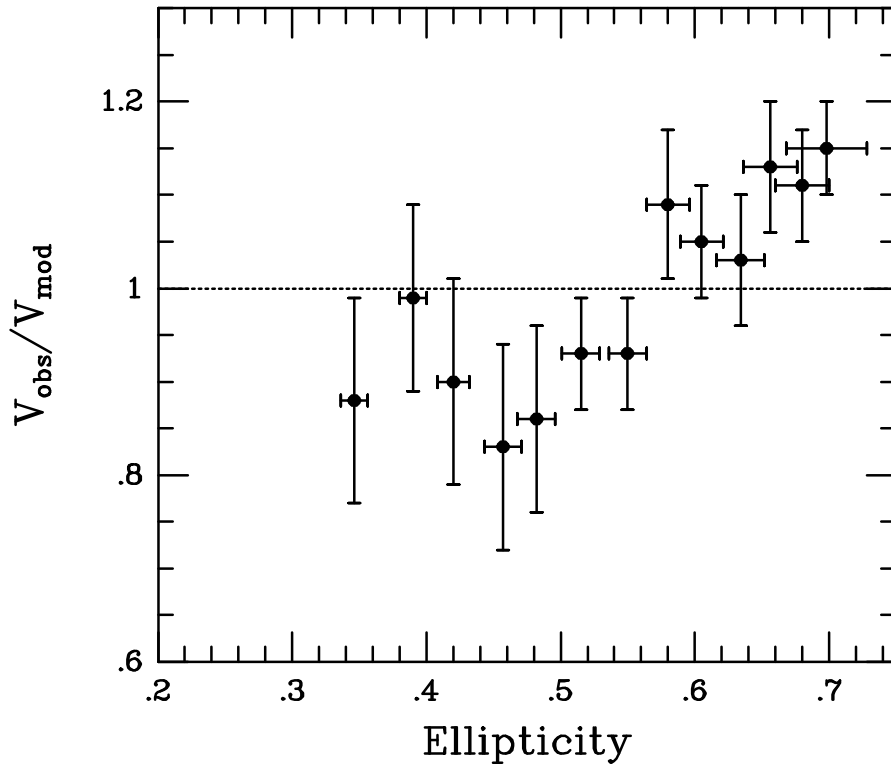


Figure 4

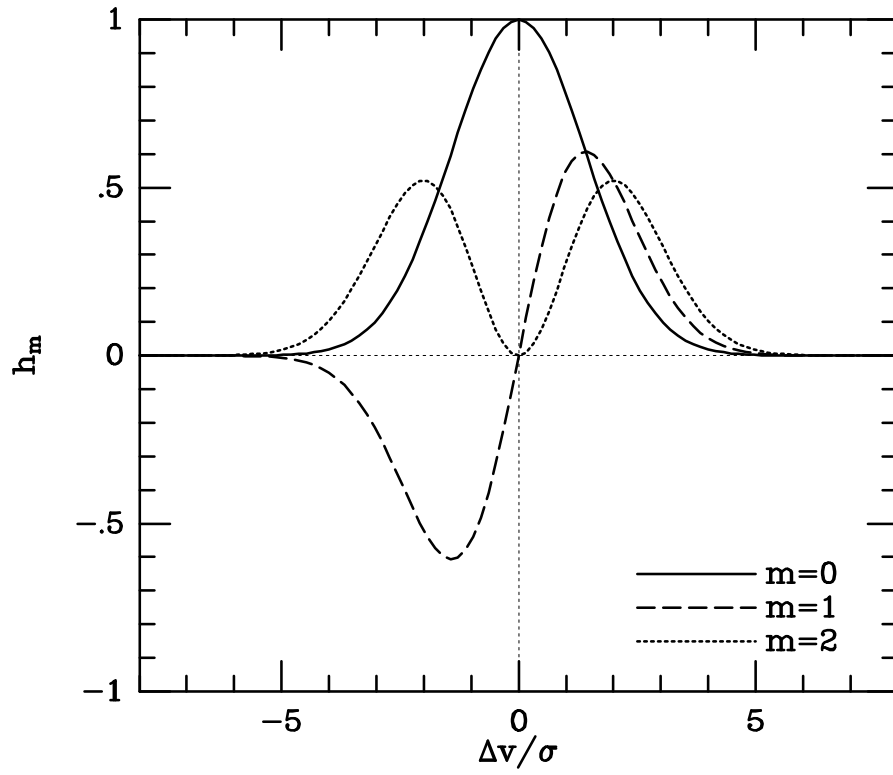


Figure 5

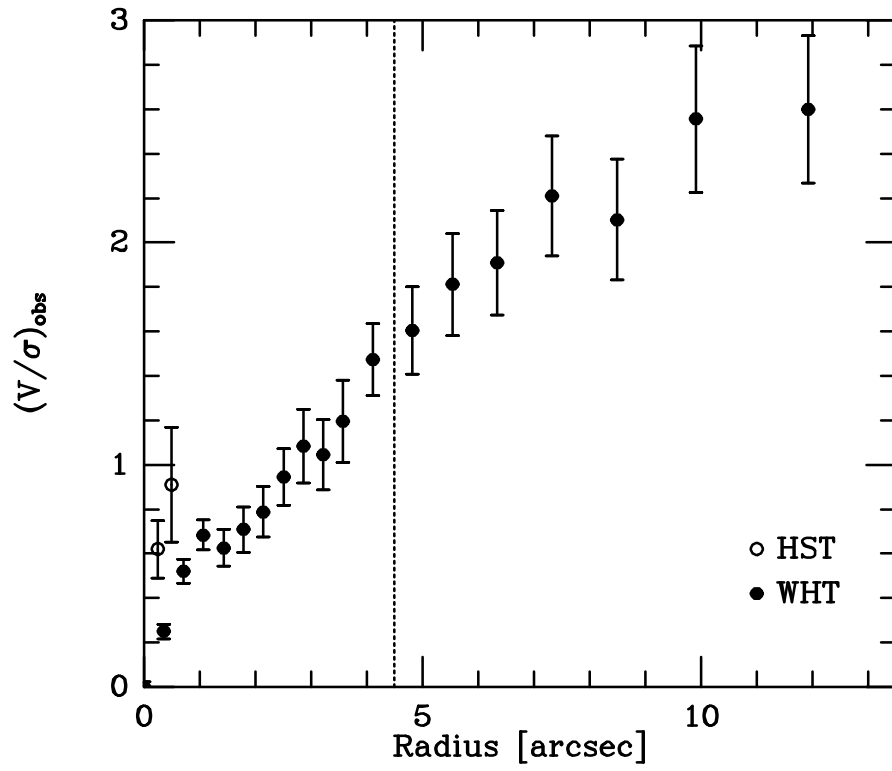


Figure 6

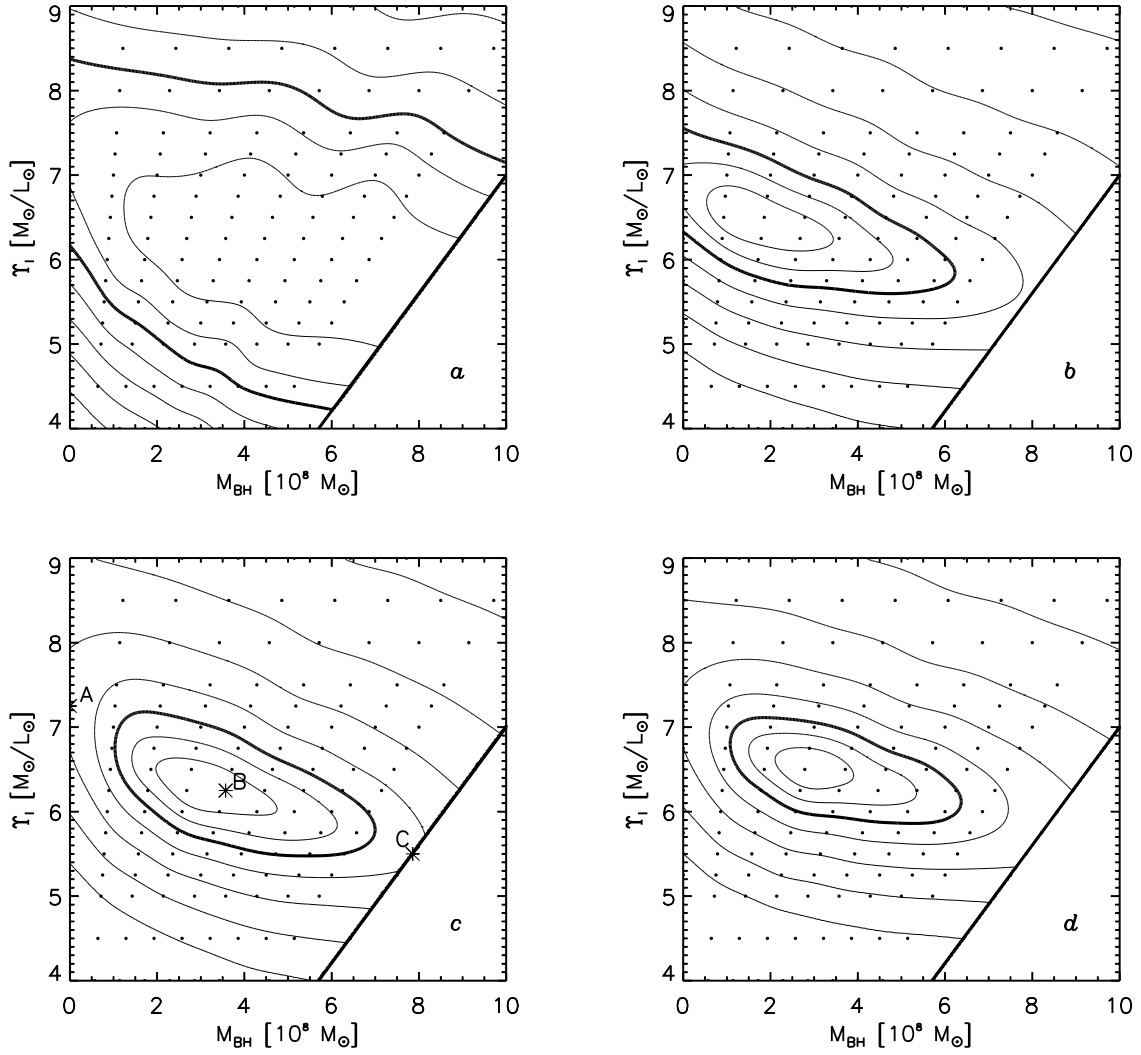


Figure 7

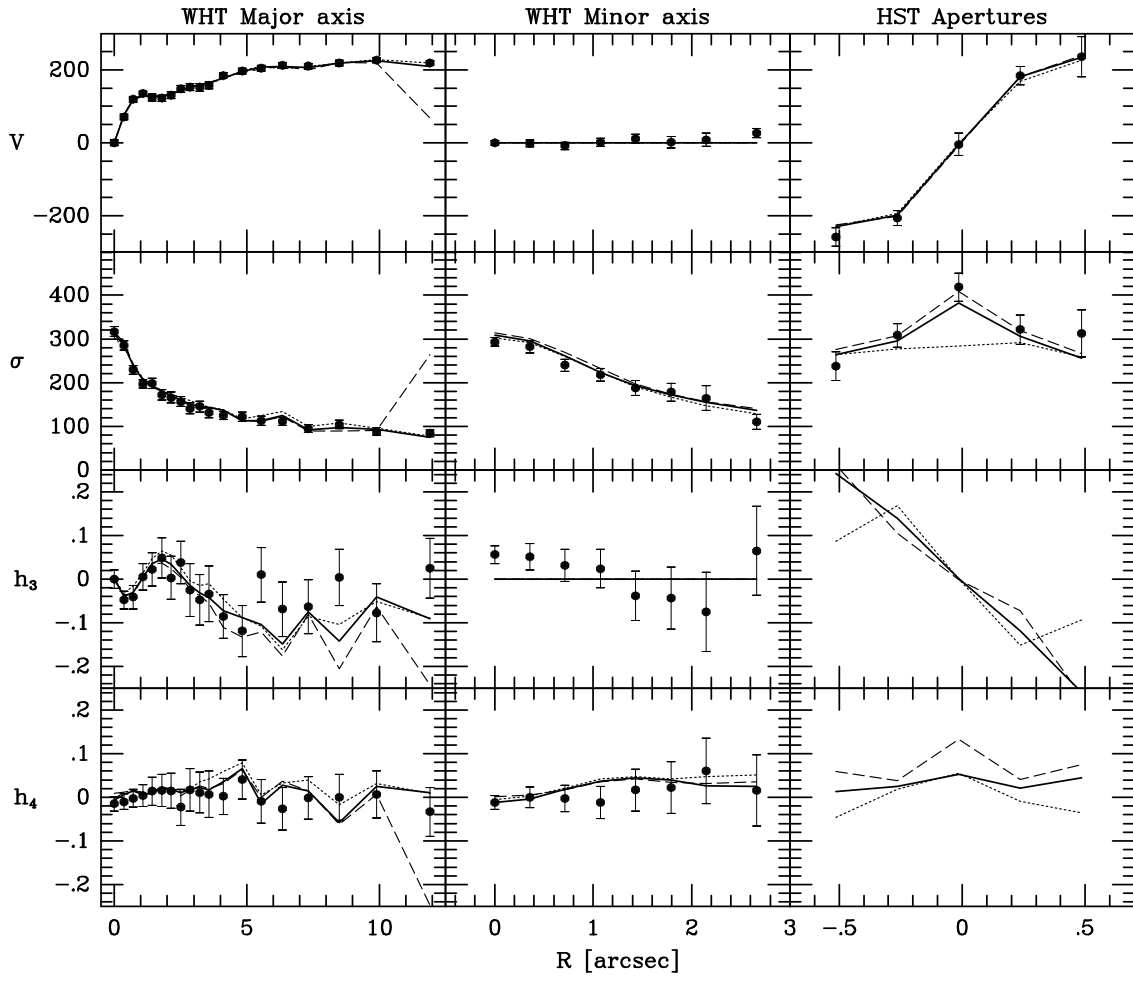


Figure 8

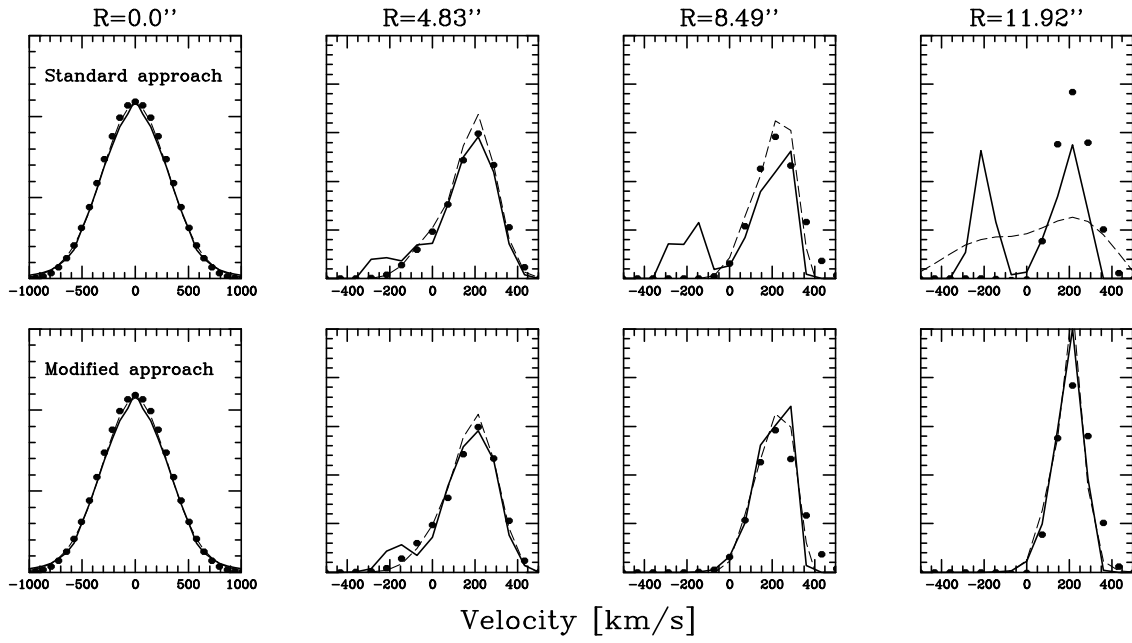


Figure 9

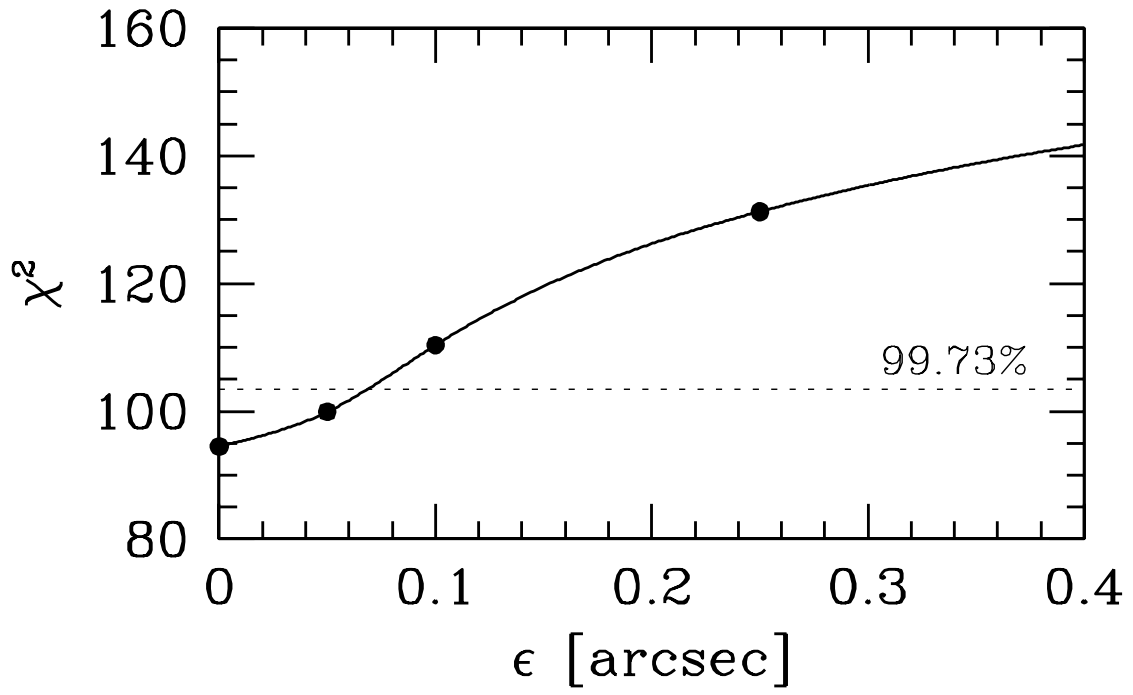


Figure 10

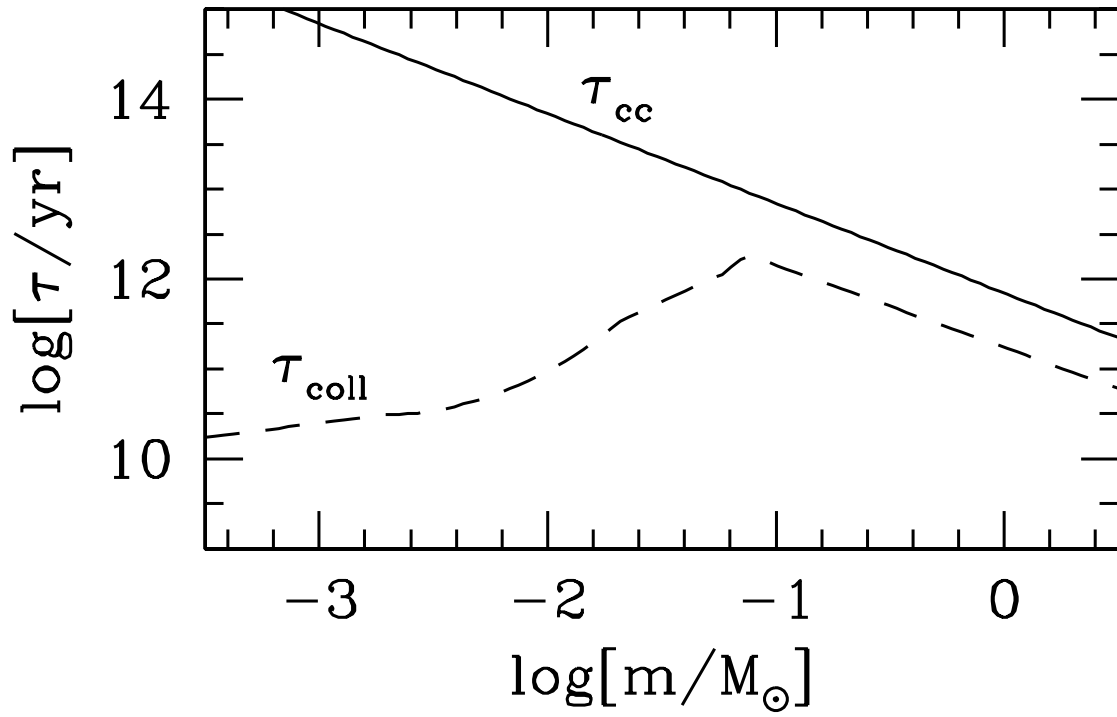


Figure 11

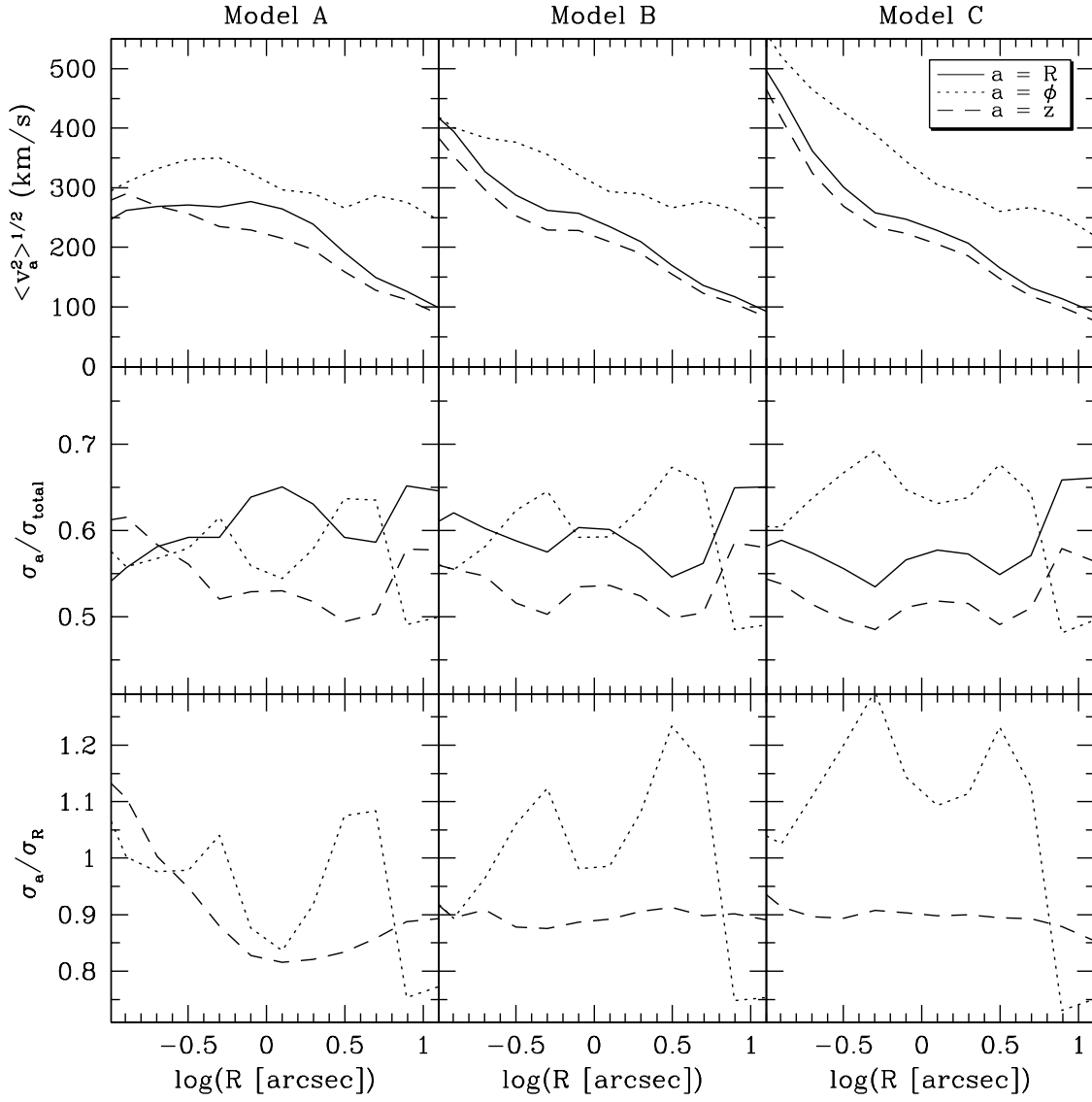


Figure 12

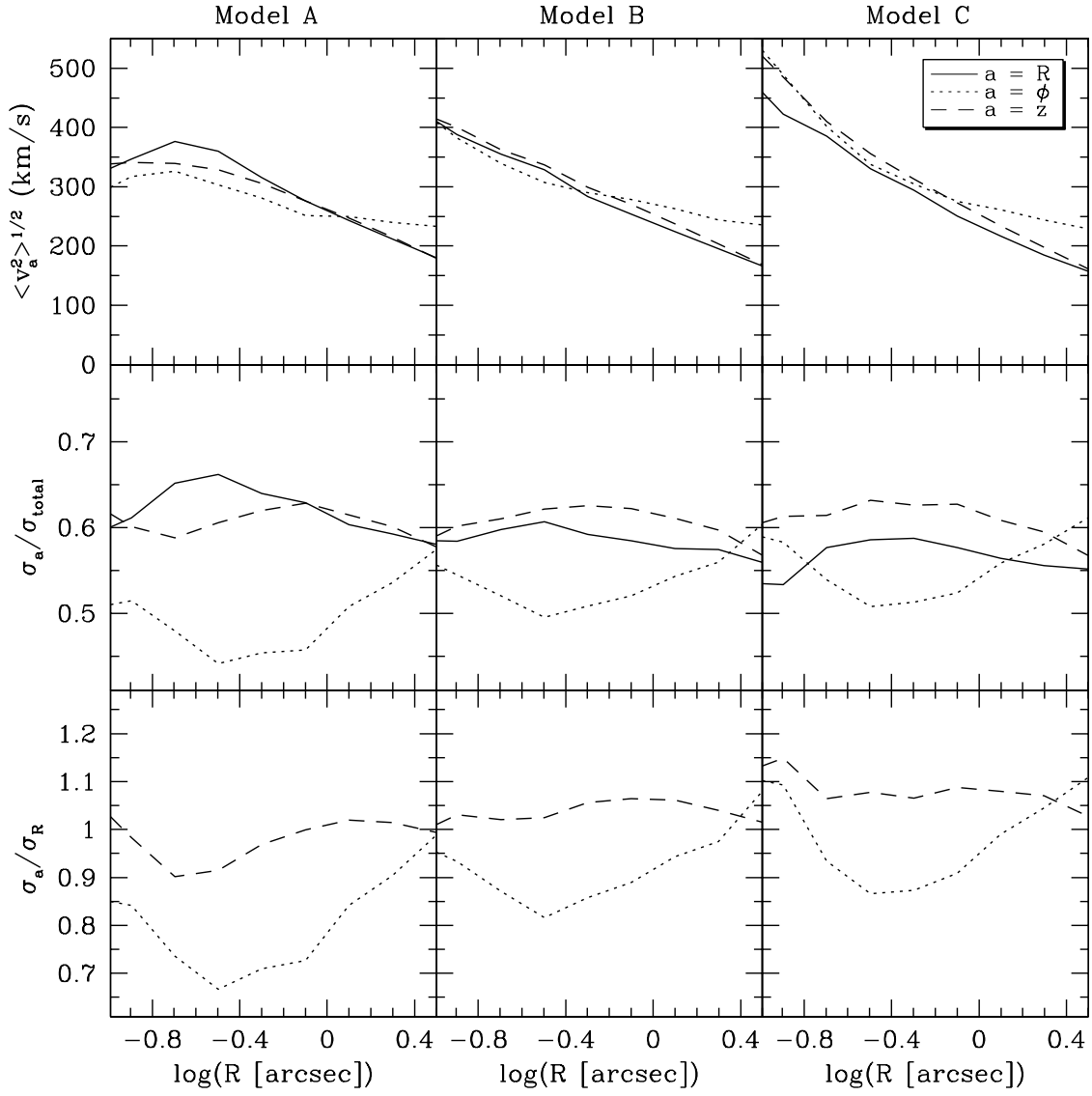


Figure 13

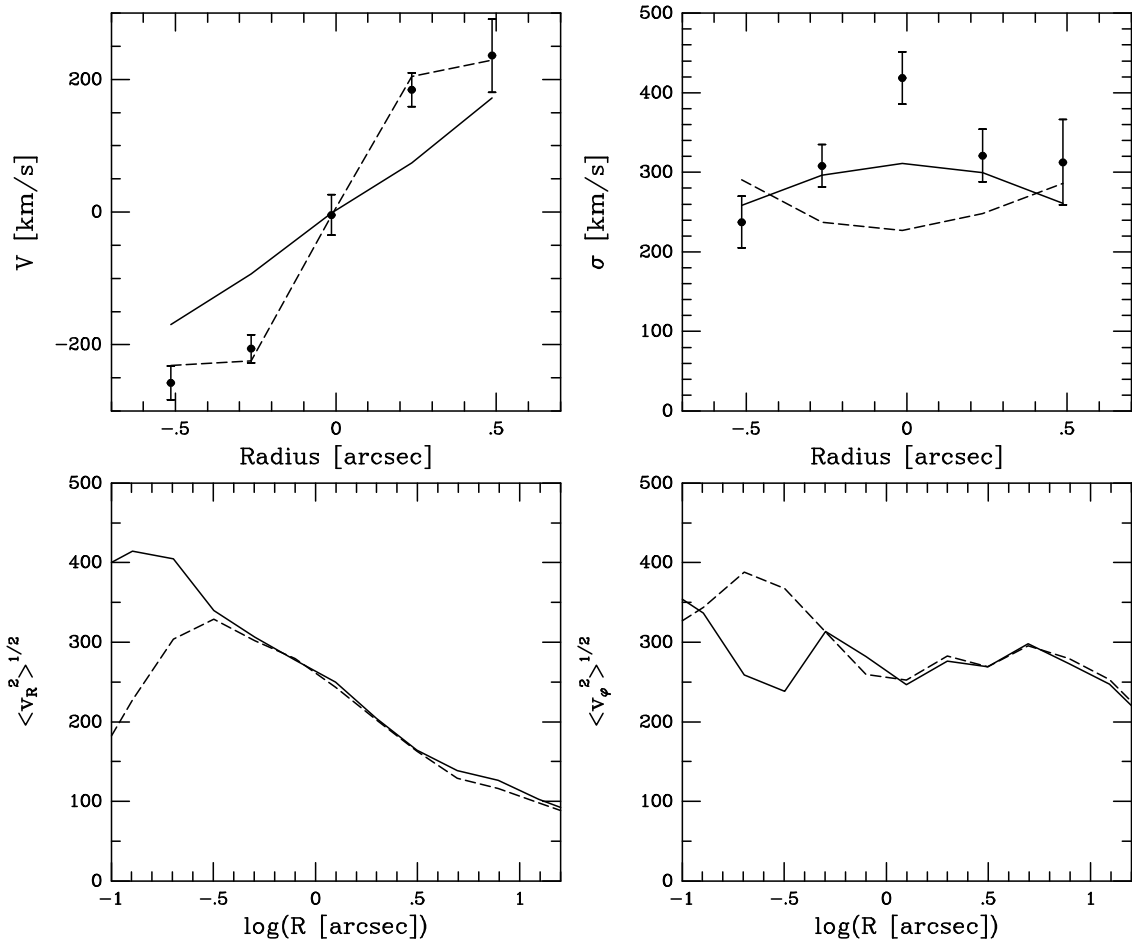


Figure 14

Table 1. Parameters of MGE model for the deconvolved I -band surface brightness.

j (1)	I'_j (2)	a'_j (3)	q'_j (4)	$L_{I,j}$ (5)
1	490833.0	0.032	0.817	1.40×10^7
2	99417.9	0.101	0.865	2.92×10^7
3	67415.3	0.282	0.601	1.07×10^8
4	84108.1	0.343	0.136	4.47×10^7
5	28511.8	0.394	0.856	1.26×10^8
6	15529.3	0.753	0.622	1.82×10^8
7	8490.8	0.756	1.000	1.61×10^8
8	6055.4	1.866	0.665	4.66×10^8
9	2951.4	4.419	0.250	4.79×10^8
10	1572.8	9.229	0.266	1.18×10^9
11	229.9	11.854	0.723	7.76×10^8

Note. — Column (1) gives the index number of each Gaussian. Column (2) gives its central surface brightness; column (3) its standard deviation (which expresses the size of the Gaussian along the major axis); column (4) its flattening; and column (5) its total I -band luminosity. All Gaussians have the same position angle and the same center.